Gaseous Flow in Micron-Sized Channels

by

Errol B. Arkilic

Submitted to the Department of Aeronautics and Astronautics
in partial fulfillment of the requirements for the degree of

Master of Science

at the

MASSACHUSETTS INSTITUTE OF TECHNOLOGY

January 1994

© Massachusetts Institute of Technology 1994. All rights reserved.

Author ....
Department of Aeronautics and Astronautics
January 28, 1994

Certified by ....
Kenneth S. Breuer
Assistant Professor of Aeronautics and Astronautics
Thesis Supervisor

Certified by 1/27/94
Martin A. Schmidt
Associate Professor of Electrical Engineering and Computer Science
Thesis Supervisor

Accepted by ....
Professor Harold Y. Wachman
Chairman, Departmental Committee on Graduate Students

MASSACHUSETTS INSTITUTE
OF TECHNOLOGY

FEB 17 1994

LIBRARIES
ARCHIVES

Gaseous Flow in Micron-Sized Channels

by

Errol B. Arkilic

Submitted to the Department of Aeronautics and Astronautics
on January 28, 1994, in partial fulfillment of the
requirements for the degree of
Master of Science

Abstract

MicroElectroMechanical Systems possess geometric features on the order of tens of microns and smaller. Because these systems have length scales comparable to the mean free path of the gaseous environments in which they reside, the exchange of energy and momentum between these systems and their environments exhibit characteristics that can be attributed to the breakdown of the environment's continuum assumption. In order to study this phenomena, an investigation into gaseous flow through micron-sized channels is undertaken. First, a model is derived that incorporates a slip-flow boundary condition and predicts an increase in the mass flow for given inlet and outlet pressures. Channels are then fabricated using photolithographic techniques of micromachining for the purposes of measuring the mass flow and pressure characteristics. A comparison between the flow results and the slip-flow model is made and it shows, for microchannels that have appreciable Knudsen numbers based on the channel height, that the no-slip boundary condition fails to accurately model the flow.

Thesis Supervisor: Kenneth S. Breuer
Title: Assistant Professor of Aeronautics and Astronautics

Thesis Supervisor: Martin A. Schmidt
Title: Associate Professor of Electrical Engineering and Computer Science

Acknowledgements

Support for this work was provided under ARPA contract #J-FBI-92-196 and through Marty Schmidt's NSF Presidential Young Investigators award.

Foremost among the people I have to thank for support throughout the work of this thesis are Kenny Breuer and Marty Schmidt. I consider them friends and mentors; their understanding and willingness to support and encourage me has had a great impact upon me and my studies. Thank you both.

In the microfabrication area, many people have been helpful. I am thankful to Ted Bloomstein, Charles Hsu, John Gilbert, Howard Goldberg, Lalitha Parameswaran and Vince McNeil for their help in teaching me microfabrication skills (special thanks to John and Lalitha for their seemingly infinite patience). Also, Pat Varley and Liz Zotos deserve thanks for their outstanding administrative support.

Beth Grimaldi, Aravind Padmanabhan, Ruben Rathnasingham, and Ravi Srinivasan have been willing to listen to my hair-brained schemes, and comment accordingly. I thank them for this.

Finally, I acknowledge the contribution of my family. My parents have unfailingly provided me with support (of all types) throughout the years and, *if* anything good can be said about me, it can be attributed to the example they provided. Victor, Dennis, Layla and Marty also have been instructive and supportive throughout the years. The most important thanks however, goes to my wife. She has put up with, among other things, more than her fair share of my late nights and weekends at the lab, and has done so with love and understanding. Thank you, Kerri.

"Rabbit's clever," said Pooh thoughtfully.

"Yes," said Piglet. "Rabbit's clever."

"And he has Brain."

"Yes," said Piglet, "Rabbit has brain."

There was a long silence.

"I suppose," said Pooh, "that that's why he never understands anything."

-A.A. Milne, *The House At Pooh Corner*

Contents

1 **Introduction** 10

1.1 Motivation 10

1.2 Non-Continuum Gas Dynamics 11

1.3 Thesis Overview 12

2 **Theory** 13

2.1 The Surface-Fluid Interaction 13

2.1.1 Accommodation Coefficients 14

2.1.2 Force Balance and the Slip Velocity 16

2.2 The Knudsen Number 18

2.3 Flow Model 19

2.3.1 Assumptions 19

2.4 Analysis 23

3 **Experimental Procedure** 27

3.1 Channel Design 27

3.1.1 Sumps 29

3.1.2 Wafer Layout 30

3.2 Channel Fabrication 32

3.2.1 Fabrication - Plasma Procedure 32

3.2.2 Fabrication Results - Plasma Procedure 35

3.2.3 Fabrication - Oxide Procedure 36

3.2.4 Fabrication Results - Oxide Procedure 38

3.3 Mounting Hardware 40
3.3.1 Pressure Chuck 44
3.4 Mass Flow Measurement 45
3.5 Pressure Measurement 48
3.5.1 Deflection Measurement 49

4 Results and Discussion **52**
4.1 Physical Parameters 52
4.2 Mass Flow Measurements 53
4.3 Knudsen Number 55
4.4 Assumption Verification 56
4.5 Comparison with Theory 57

5 Conclusions **62**

A Process Travelers **65**

B Masks **71**
B.1 Mask 1 71
B.2 Mask 2 71
B.3 Mask 3 74

List of Figures

2-1 Molecules reflecting from specularly reflective surfaces behave like photons reflecting from flat mirrors 15

2-2 Molecules reflecting from diffuse surfaces have a reflection distribution 15

2-3 Model used to derive the slip velocity 17

2-4 Geometry for two-dimensional microchannel flow 20

3-1 Exploded view of a typical micromachined channel 28

3-2 Cross sectional view of capping wafer deflection 29

3-3 The wafer is divided into nine separate regions 31

3-4 Channel wafer fabrication sequence - plasma procedure 33

3-5 Capping wafer fabrication sequence - plasma procedure 34

3-6 Bonded wafer fabrication sequence - plasma procedure 35

3-7 Surface profile of channel face - plasma procedure 37

3-8 Channel wafer fabrication sequence - oxide procedure 39

3-9 Bonded wafer fabrication sequence - oxide procedure 40

3-10 Surface profile of channel face - oxide procedure 41

3-11 Exploded view of initial wafer chip and mounting hardware 42

3-12 Exploded view of final wafer chip and mounting hardware 43

3-13 Features of the pressure chuck 44

3-14 Test platform 47

3-15 Surface deflection of capping wafer at pressure 50

3-16 Calibration results for sump response 51

4-1 Typical differential pressure signal as a function of time for one channel test 54
4-2 Mass flow as a function of pressure ratio 55
4-3 Inlet and outlet Knudsen number as a function of pressure ratio . . . 56
4-4 A comparison between the flow data normalized by the no-slip solution and Equation 2.35 for $F = 1$ 58
4-5 A comparison between the flow data normalized by the no-slip solution and Equation 2.35 for various values of F 60
4-6 A comparison between the flow data normalized by the no-slip solution and Equation 2.35 utilizing the values of Table 4.2 and $F = 0.54$ . . . 61

5-1 To measure the pressure distribution, pressure taps can be included down the length of the channel 63

B-1 Mask 1 used to define channel geometry 72
B-2 Mask 2 used to define the back side ports 73
B-3 Mask 3 designed for identification marks 74

List of Tables

3.1 Channel specification of wafer regions 31

3.2 Results from plasma fabrication procedure 36

3.3 Results from oxide fabrication procedure 40

4.1 Values of physical parameters 52

4.2 One set of parameters that can be used to model the experimental data 61

Chapter 1

Introduction

1.1 Motivation

MicroElectroMechanical Systems (MEMS) is an emerging technology that incorporates some of the fabrication techniques long associated with integrated chip manufacturing. Unlike integrated circuitry, these systems are designed to mechanically interact with their environment. These interactions are brought about by the exchange of energy and momentum between the systems and their environments. What makes the exchange for MEMS interesting is the scale of these systems; MEMS commonly possess geometric features on the order of tens of microns and smaller[1]. As the system dimensions decrease and approach the order of the molecular mean free path of the gaseous environment, the exchange of energy and momentum with the surrounding gas will exhibit behavior that is not typically witnessed on the macro-level.

Because MEMS are typically immersed in a fluid environment, successful modeling of these systems will rely upon the ability to accurately model fluid phenomena on the micron scale. On this scale, the fluid dynamics exhibit properties that can be attributed to the underlying molecular composition of the fluid; a continuum analysis of the flow may not be accurate.

[1] A typical human hair has a diameter of 50 μm

1.2 Non-Continuum Gas Dynamics

It is known that all gases have a discreet molecular composition, yet, seldom is this nature of a gas directly modeled. Instead, the effects of the molecular composition are parameterized into the gas fundamental properties which include: density, viscosity, thermal conductivity and specific heat. Further investigation into fluid phenomena is then based on the governing differential equations which assume continuous behavior of the properties (the continuum assumption). The equations are derived from the conservative properties of mass, energy and momentum. In order to solve them, boundary conditions that give the flow characteristics at the solution boundary, must be imposed. A typical boundary condition that is used to model the velocity at a solid-fluid interface is such that the normal and tangential components of the velocity, with respect to the solid boundary, are zero. For the majority of flow situations, the zero-velocity, or no-slip, model represents the momentum transfer accurately. However, as the mean free path becomes comparable to the geometric scale of the physical system, as when the gas is rarefied, the exchange of properties between systems and their fluid environment can no longer be based on the continuum differential equations. It is known that in a low density gas of sufficient rarefaction the effects of the breakdown of the continuum assumption can be witnessed [1]. Historically, non-continuum gas dynamics has been studied where the working fluids exhibit low density such as in the flow through vacuum systems and around flight vehicles at high altitudes. The features commonly possessed by these seemingly disparate types of flow include the rarefaction of the working fluid and, more importantly, the ratio of the molecular mean free path of the working fluid to the governing length scale of the flow.

For a typical diatomic gas, nitrogen N_2, the mean free path at standard atmospheric conditions is approximately 70 nm. Based on a similarity analysis, one would expect flow fields that possess characteristic dimensions of comparable order to demonstrate non-continuum effects, even though by common standards the density of the gas at standard conditions does not exhibit rarefaction. It is believed that the internal and external flow fields of MEMS can display non-continuum effects. In fact

there is experimental evidence[2] which suggests that gas flow through micron sized channels may exhibit the essence of non-continuum flow, which is characterized by a decrease in the shear at the channel wall.

The ratio of the molecular mean free path of the working fluid to the governing length scale of the flow is called the Knudsen number, Kn; it is the parameter that characterizes the breakdown of the continuum assumption.

1.3 Thesis Overview

In this thesis, it is shown that internal microfluid flow can achieve appreciably high Knudsen numbers ($Kn > 0.01$). An analytical model for the mass flow as a function of the inlet and outlet pressures for channel flow that is functionally dependent on the Knudsen number is derived in Chapter 2. The momentum exchange predicted by this model deviates from the classical theory and the deviation is such that a decrease in the momentum exchange between the wall and the fluid is predicted. In order to verify this model, a simple flow experiment is carried out on a microchannel.

The microchannel flow experiment is conducted in a silicon micromachined channel which is pressurized with nitrogen. The fabrication sequence used in the making of the small silicon channels, as well as the experimental regimen, is related in Chapter 3. The experimental procedure used to test the flow through the microchannel demonstrates the feasibility of an on-chip optical pressure measurement technique and introduces a technique that can be used for sensitive mass flow measurement[2]. Results and discussion of the experiment are given in Chapter 4, with conclusions in Chapter 5.

---

[2]In this study mass flows on the order of ng per second are common.

Chapter 2

Theory

2.1 The Surface-Fluid Interaction

When gas molecules impinge upon a surface, the simplest kinetic model states that the molecules exchange two properties with the surface: energy and momentum. The extent to which impinging molecules reach equilibrium with the surface is parameterized in the accommodation coefficients. For example, if on average, the impinging molecules are rebounded with the same energy and momentum as the wall, the molecules are said to be fully accommodated.

Because there are two properties exchanged at the wall, there are two accommodation coefficients. The coefficients are usually empirically determined, and are functions of both the surface and the gas. The energy accommodation coefficient is usually called the thermal accommodation coefficient or, simply, the accommodation coefficient. The coefficient that characterizes the exchange of momentum is called the momentum accommodation coefficient or, more frequently, the specular reflection coefficient.

2.1.1 Accommodation Coefficients

The thermal accommodation coefficient is defined by:

$$A \equiv \frac{T_r - T_i}{T_w - T_i}, \tag{2.1}$$

where

T_r = average temperature of the reflected molecules,

T_i = average temperature of the incident molecules,

T_w = average wall temperature.

In this study there is no effort to heat or cool the wall of the microchannel and it is assumed that the flow is isothermal (see Section 2.3.1). Therefore, it is assumed that $T_r = T_w$ and the thermal accommodation is complete, with a coefficient of 1. Further investigation is required to determine the impact of thermal accommodation on microchannel flows.

The specular reflection coefficient is defined by:

$$F \equiv \frac{u_r - u_i}{U_w - u_i}, \tag{2.2}$$

where

u_r = average streamwise velocity of the reflected molecules,

u_i = average streamwise velocity of the incident molecules,

U_w = average streamwise velocity of the surface.

Among the important characteristics, in determining the specular reflection coefficient of a surface-gas interface, are the roughness of the surface and the species of the impinging gas molecules. If the surface were smooth on the molecular length scale of the incident gas particles, the reflections would be perfectly specular (see Figure 2-1). In perfectly specular reflections, molecules transfer no streamwise momentum to the walls; this implies that the incident streamwise velocity is equal to the reflected streamwise velocity, $u_i = u_r$. Therefore, by Equation 2.2, a perfectly specular surface has $F = 0$. Because the angle of incidence is equal to the angle of

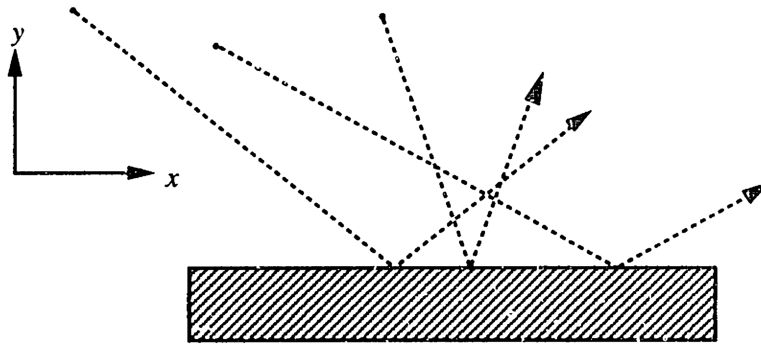

Figure 2-1: Molecules reflecting from specularly reflective surfaces behave like photons reflecting from flat mirrors

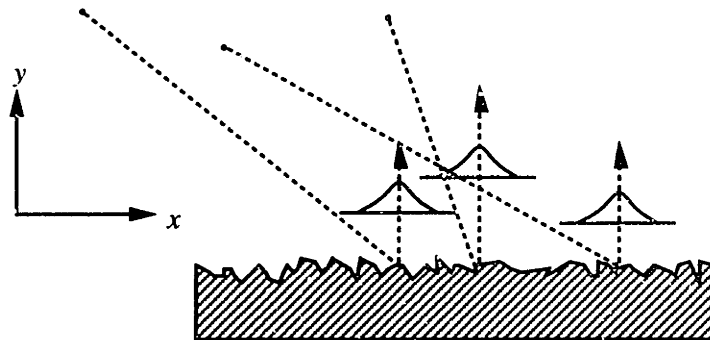

Figure 2-2: Molecules reflecting from diffuse surfaces have a reflection distribution

reflection for specular reflections, they are often likened to light reflections from a flat mirror. If the surface were rough, on the molecular length scale of the gas particles, the reflections would be diffuse. Diffuse reflections are characterized by a complete transfer of streamwise momentum from the molecules to the wall. As with other kinetic properties of a gas, there is a distribution of the reflected velocities, but, on average, $u_r = U_w$ for diffuse surface-gas interactions and $F = 1$ (see Figure 2-2).

It must be kept in mind that the specular reflection coefficient is a function of the surface as well as the gas. Also, there is evidence that the surface dependence is more than just geometrically based [3]; the molecular species absorbed on the surface also seems to influence the specular reflection coefficient.

Like the thermal accommodation coefficient, A, the specular reflection coefficient, F, is usually determined empirically. For most engineering surfaces, values for F are near unity [4], though for certain gas-surface interactions values as low as 0.20 have

been reported [5].

2.1.2 Force Balance and the Slip Velocity

The kinetic theory of gases states that, as gas molecules collide with a wall, the streamwise momentum transferred to the wall appears in the continuum as a shear force at the wall.[1] In order to equate the shear at the wall to the average momentum transferred to the wall per unit area per unit time, the following expressions are needed: the number of molecules incident on a unit area of wall per unit of time, the average streamwise momentum with which each molecule arrives at the wall and the fraction of momentum the gas molecules exchange on average.

The fraction of momentum transferred to the wall is given by the specular reflection coefficient, F. The number of molecules incident on the wall per unit of area per unit of time, N, for a gas with a Maxwellian velocity distribution is given by [6]:

$$N = \frac{\bar{c}P}{4\kappa T}, \tag{2.3}$$

where

$$\begin{aligned} \bar{c} &= \text{mean speed of particles,} \\ P &= \text{pressure,} \\ \kappa &= \text{Boltzmann constant,} \\ T &= \text{gas temperature.} \end{aligned}$$

Now, an expression for the momentum with which the molecules arrive is needed. Throughout the flow, there exists some velocity gradient $\frac{\partial u}{\partial y}$ that, in general, is a function of position (x,y,z) and time (t). However, if the flow is fully developed, incompressible, steady and two-dimensional (which is discussed in Section 2.3.1), then $\frac{\partial u}{\partial y} = \frac{du}{dy}$. Molecules that collide with a wall come from a distance $2/3\Lambda$ away [7]. Λ is the mean free path and is given by:

$$\Lambda = \frac{\kappa T}{P\sigma^2\pi\sqrt{2}}, \tag{2.4}$$

[1] The exchange of normal momentum appears as pressure.

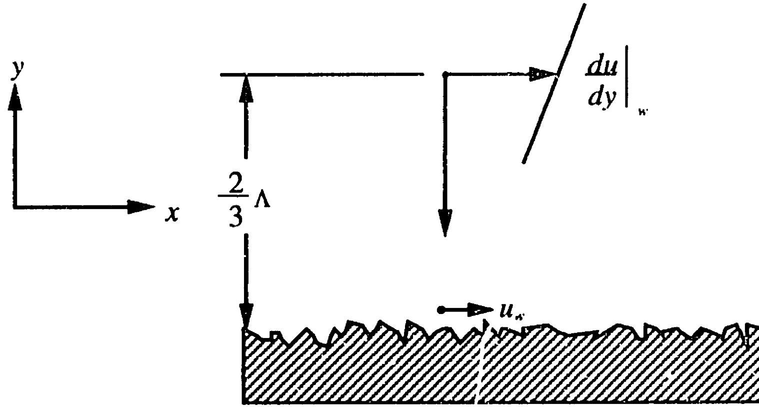

Figure 2-3: Model used to derive the slip velocity

where

$$\sigma = \text{molecular diameter.}$$

The easiest approach to show the existence of the wall slip velocity, u_w, is to assume that it exists and then to show demonstratively that it is nonzero. Following this procedure and assuming a linear velocity gradient, the momentum with which each molecule arrives at the surface is given by:

$$m(u_w + \frac{2}{3}\Lambda \left.\frac{du}{dy}\right|_w), \tag{2.5}$$

where

$$\begin{aligned} m &= \text{mass of molecule,} \\ u_w &= \text{velocity near the wall, slip velocity,} \\ \left.\frac{du}{dy}\right|_w &= \text{gradient of the velocity at the wall.} \end{aligned}$$

The shear is equal to the number of molecules per unit area per unit time, N, transferring a fraction, F, of their momentum. Therefore:

$$FNm(u_w + \frac{2}{3}\Lambda \left.\frac{du}{dy}\right|_w) = \mu \left.\frac{du}{dy}\right|_w . \tag{2.6}$$

Where an expression for μ can be written as [8]:

$$\mu = 0.499\frac{m\bar{c}}{\sigma^2\pi\sqrt{2}}. \tag{2.7}$$

With the expressions for μ and N, the slip velocity can be found to be given by:

$$\frac{5.988 - 2F}{3F}\Lambda\left.\frac{du}{dy}\right|_w. \tag{2.8}$$

A similar but more refined analysis was given by Maxwell [6], who found that:

$$u_w = \frac{2 - F}{F}\Lambda\left.\frac{du}{dy}\right|_w. \tag{2.9}$$

A non-dimensional form of the wall slip velocity can be written as:

$$\frac{u_w}{U_0} = \frac{2 - F}{F}\frac{\Lambda}{H}\left.\frac{d\frac{u}{U_0}}{d\frac{y}{H}}\right|_w, \tag{2.10}$$

where

$$\begin{aligned} H &= \text{characteristic dimension,} \\ U_0 &= \text{characteristic velocity.} \end{aligned}$$

Equation 2.10 demonstrates that every gas flow possesses a slip at the wall; for all viscid gas flows, the velocity gradient is nonzero. What governs the order of the slip velocity is the ratio of the mean free path to the characteristic flow dimension.

2.2 The Knudsen Number

The ratio of the mean free path to characteristic flow dimension is called the Knudsen number, Kn and is the parameter used in the study of non-continuum gas dynamics to characterize the breakdown of the continuum assumption. The Knudsen number based on a characteristic dimension is defined by:

$$Kn = \frac{\Lambda}{H}. \tag{2.11}$$

When a gas ceases to behave entirely as a continuous media, it exhibits characteristics that are derived from its discrete molecular makeup. It has been suggested that there exists 4 types of flows that can be characterized by the size of the Knudsen number [4]: continuum flow, slip flow, transition flow, and free molecular flow.

If $Kn < 0.01$, the flow is said to be in the continuum-flow regime. The Navier-Stokes equations are valid and the vast majority of studies in fluid dynamics are concerned with flow in this regime.

If $0.01 < Kn < 0.1$, the flow is said to be in the slip-flow regime. Within the slip-flow regime, the Navier-Stokes equations may be used with a boundary condition of slip at the wall.

If $0.1 < Kn < 3$, the flow is said to be in the transition regime. The transition regime does not lend itself to simple analysis and the majority of information about this regime is empirical.

If $3 < Kn$, the flow is said to be in the free molecular flow regime. Within the free molecular flow regime, intermolecular collisions are assumed to be negligible in determing the gas dynamics.

Of course, the distinctions between the flow regimes, as stated above, are not always definitive.

2.3 Flow Model

The modeled channel geometry is given in Figure 2-4. This is the model used for laminar, incompressible, steady flow between parallel plates.

The slip-velocity boundary condition at the wall on the flow profile is represented in Figure 2-4

2.3.1 Assumptions

Among the model's assumptions is that of incompressible flow. Even though there can be significant changes in the density of microchannel gas flow it will be shown that the flow is still incompressible. Also, it is assumed that the flow is isothermal.

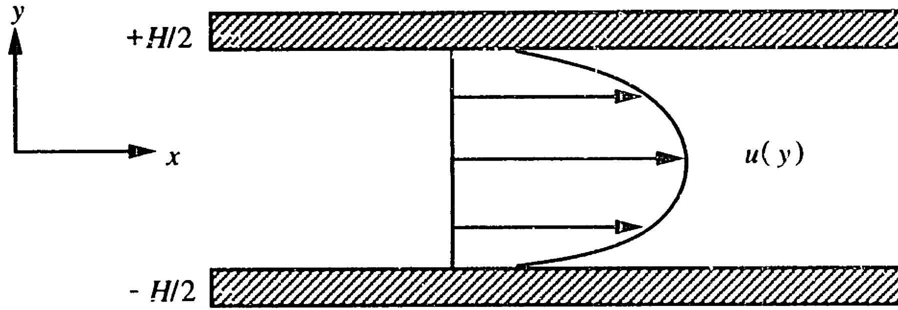

Figure 2-4: Geometry for two-dimensional microchannel flow

Because the drop in pressure is due to viscous effects and not to any free-expansion of the gas, the isothermal assumption should be valid. Another assumption that greatly simplifies matters is that of two-dimensional flow. If the aspect ratio of the channel is large, then the cross-width gradients can be ignored.

Incompressible Flow

If the change in local density is small enough as to be negligible, then the assumption of incompressible flow is justified. This implies that, in order for an incompressible model to be valid,

$$\frac{\delta\rho}{\rho} \ll 1, \tag{2.12}$$

where

$$\begin{aligned} \delta\rho &= \text{change in local density,} \\ \rho &= \text{local density.} \end{aligned}$$

By looking at the force balance between pressure and inertial forces, it can be shown that [9]:

$$\frac{\delta\rho}{\rho} \sim Ma^2, \tag{2.13}$$

where

$$Ma = \text{Mach number.}$$

If the pressure forces are in equilibrium with the inertial forces, the requirement for incompressible flow is that:

$$Ma^2 \ll 1. \tag{2.14}$$

This is the well-established criterion for incompressible flow of gases. However, for microflows of the type dealt with here, there is a more stringent requirement. The force balance is between the viscous and pressure forces and a simple analysis reveals [9]:

$$\frac{\delta\rho}{\rho} \sim \frac{Ma^2}{Re}, \tag{2.15}$$

where

Re = Reynolds number based on some characteristic dimension.

In order to satisfy the incompressible flow criterion, it is therefore necessary that:

$$\frac{Ma^2}{Re} \ll 1. \tag{2.16}$$

If one utilizes the definition of Kn and the equation for viscosity (Equations 2.11 and 2.7), the above criterion can be recast into:

$$MaKn \ll 1. \tag{2.17}$$

Because there is a significant decrease in the pressure along the length of a microchannel, microchannel flow is not constant density flow. However, under certain circumstances, the flow can be modeled as incompressible, namely when the product of the Mach number and Knudsen number or when the ratio of the square of the Mach number and the Reynolds number are small compared to unity.

Isothermal Flow

The motivation for modeling the flow as isothermal relies on the simplicity afforded the equation of state. When the flow is isothermal, the density is simply proportional to the pressure and the analysis is simplified. It can be shown that for long uninsulated pipes, the criterion for isothermal flow is [10]:

$$Ma \ll \frac{1}{\sqrt{\gamma}}, \tag{2.18}$$

where

$$\gamma = \text{ratio of specific heats.}$$

Silicon is a good thermal conductor and because the thermal entrance length is comparable in size to the flow entrance length, any channel that can be modeled as fully developed will also be assumed 'long' for the purposes of the isothermal criterion, Equation 2.18.

Fully Developed Flow

At the inlet and outlet there are pressure losses associated with the constriction and expansion of the flow. By stating that the flow is fully developed, it is implied that the entrance lengths and the effects on pressure drop are small enough as to be negligible. The order of the pressure losses at the inlet and outlet is given by[11]:

$$\mathcal{O}(\Delta P_{entrance}) = \frac{\rho U_0^2}{2}. \tag{2.19}$$

The order of the pressure loss due to viscosity along the length of an internal flow is given by:

$$\mathcal{O}(\Delta P) = \frac{2\mu L U_0 (w+H)^2}{(wH)^2}, \tag{2.20}$$

where

$$H = \text{channel height,}$$
$$L = \text{length of channel,}$$
$$w = \text{width of channel.}$$

To be able to ignore the losses associated with the inlet and exit of the channel, $\mathcal{O}(\Delta P_{entrance}) \ll \mathcal{O}(\Delta P)$, or:

$$\frac{\rho U_0^2}{2} \ll \frac{2\mu L U_0 (w+H)^2}{(wH)^2}. \tag{2.21}$$

By multiplying both sides by the area, it can be shown that in order to neglect inlet losses:

$$\dot{m} \ll \mathcal{O}\left(\frac{4\mu L (w+H)^2}{wH}\right). \tag{2.22}$$

Two-Dimensional Flow

In assuming a two-dimensional flow it is accepted that there are no important flow gradients in the z-dimension, i.e,

$$\frac{\partial}{\partial z} = 0. \tag{2.23}$$

Another way of expressing the two dimensional criteria is by looking at the flow solution for a three-dimensional analysis. It can be shown that the flow rate through a three-dimensional duct is given to the leading order by [1]:

$$Q_{3d} \sim Q_{2d}\left(1 - \frac{1}{\mathit{AR}^2}\right), \tag{2.24}$$

where

$$\begin{aligned} Q_{2d} &= \text{the flow rate from a two-dimesional analysis,} \\ \mathit{AR} &= \text{aspect ratio.} \end{aligned}$$

For large aspect ratio channels, difference in the flow rates between a two and three-dimensional analysis should be negligible.

2.4 Analysis

The governing equations for this study include the constant viscosity incompressible momentum equations (Navier-Stokes equations), the incompressible mass continuity equation, and the ideal equation of state. These equations, along with the slip boundary condition derived in Section 2.1.2, allow for an analysis of the microchannel flow.

The Navier-Stokes equations, ignoring gravitational effects are:

$$\rho\frac{D\vec{u}}{Dt} = -\nabla P + \mu\nabla^2\vec{u}. \tag{2.25}$$

The incompressible continuity equation is:

$$\nabla\vec{u} = 0. \tag{2.26}$$

The equation of state is:

$$P = \rho RT, \tag{2.27}$$

where

$$\vec{u} = \text{velocity},$$
$$R = \text{specific gas constant},$$

For two-dimensional flow, the Navier-Stokes and continuity equations reduce to:

$$\frac{dP}{dx} = \mu \frac{d^2u}{dy^2}. \tag{2.28}$$

The boundary conditions, for the above equation are:

$$y = \pm H/2; \quad u = u_w = \tfrac{2-F}{F} \Lambda \tfrac{du}{dy} \mid_{\pm H/2},$$

With these boundary conditions, Equation 2.28 can be integrated twice with respect to y to obtain:

$$u = \frac{1}{2\mu}\frac{dP}{dx}\left(y^2 - \frac{H^2}{4} - \frac{2-F}{F}H^2 Kn\right). \tag{2.29}$$

The average velocity, u_A, is found by integrating across the channel depth:

$$u_A = \frac{1}{H}\int_{-H/2}^{H/2} u(y)dy = -\frac{H^2}{12\mu}\frac{dP}{dx}\left(1 + 6\frac{2-F}{F}Kn\right). \tag{2.30}$$

As the flow proceeds down the channel the pressure and the density drop due to viscous dissipation and, therefore, to preserve mass continuity, the average velocity increases. Though the velocity increases, the mass flow is constant, and, utilizing the equation of state, it is found to be:

$$\dot{m} = Hw\rho u_A = -\frac{H^3 w}{12\mu RT}\frac{dP}{dx}\left(P + 6\frac{2-F}{F}KnP\right). \tag{2.31}$$

If the flow is isothermal, KnP is constant at any station along the channel and one can set KnP to Kn_oP_o, where the the subscripts refer to the properties evaluated at the channel outlet. Substituting Kn_oP_o into Equation 2.31 and integrating in x one obtains:

$$\dot{m}\frac{x}{H} = \frac{H^2 w}{12\mu RT}\left[\frac{P_i^2 - P_x^2}{2} + 6\frac{2-F}{F}Kn_oP_o(P_i - P_x)\right], \tag{2.32}$$

where

$$P_i = \text{pressure evaluated at the channel inlet,}$$
$$P_x = \text{pressure evaluated at position } x.$$

Normalizing Equation 2.32 by the outlet pressure, P_o, and letting $x = L$, the length of the channel, gives:

$$\dot{m}\frac{L}{H} = \frac{H^2 w P_o^2}{24\mu RT}\left[(\mathcal{P}_i^2 - 1) + 12\frac{2-F}{F}Kn_o(\mathcal{P}_i - 1)\right], \tag{2.33}$$

where

$$\mathcal{P}_i = \text{the ratio of inlet to outlet pressure,} \frac{P_i}{P_o}.$$

Upon examination of Equations 2.32 and 2.33, it can seen that the effect of the slip velocity presents itself in the third term of each equation. By including the slip velocity at the wall, one adds another term to the equation for the mass flow. Notice that the mass flow for a given inlet and outlet pressure always increases due to the effect of slip. This could be interpreted as an apparent reduction of the fluid viscosity. It is interesting to note that, as the inlet to outlet pressure ratio decreases, the effects of slip become a more significant contribution to the whole flow.

The solution of the above model, with the no-slip boundary condition is given by:

$$\dot{m}_{NS}\frac{L}{H} = \frac{H^2 w P_o^2}{24\mu RT}(\mathcal{P}_i^2 - 1). \tag{2.34}$$

Dividing Equation 2.33 by 2.34, we obtain:

$$\frac{\dot{m}}{\dot{m}_{NS}} = 1 + 12\frac{2-F}{F}Kn_o P_o \frac{1}{(P_i + P_o)}. \tag{2.35}$$

For a given specular reflection coefficient, F, and outlet Knudsen number, Kn_o, the deviation between the two models decreases as the pressure ratio increases.

In the limiting case, where there is no mass flow $P_i \rightarrow P_o$, the ratio between the two models becomes:

$$1 + 6\frac{2-F}{F}Kn_o. \tag{2.36}$$

For a given outlet pressure, Equation 2.36 gives the maximum deviation between the slip-flow and no-slip solutions to the Navier-Stokes equations.

In further analysis, for a given mass flow, Equation 2.32 can be solved for the pressure distribution along the length of the channel, doing this yields:

$$\mathcal{P}_x = -6Kn_0\tfrac{2-F}{F} + \sqrt{36\left(\tfrac{2-F}{F}\right)^2 Kn_o^2 + \left[\mathcal{P}_i^2 + 12\tfrac{(2-F)}{F}Kn_o\mathcal{P}_i\right](1-\tfrac{x}{L}) + \tfrac{x}{L}\left[1 + 12\tfrac{(2-F)}{F}Kn_o\right]}, \tag{2.37}$$

where

$$\mathcal{P}_x = \tfrac{P_x}{P_o}.$$

If a method could be derived of measuring the pressure distribution along the length of the channel without perturbing the flow, expression 2.37 could be used for a further analysis of microchannel flows.

Chapter 3

Experimental Procedure

3.1 Channel Design

In this study, there were four goals based on the geometry of the channel that we wished to achieve. In the order of importance they were:

1. The channels should have Knudsen numbers, based on channel height, in the range valid for the slip-flow model ($0.1 > Kn > 0.01$).
2. The two-dimensional flow requirement of Section 2.3.1 should be met.
3. The channel design should provide a means for on-chip pressure measurement.
4. The channel should allow for means to test the effects of the inlet pressure loss.

In order to achieve these goals, we utilized wafer-bonding microfabrication technology. With this technology, the channels are fabricated on one wafer (channel wafer) and a second wafer is used only to cap the channel wafer (capping wafer), see Figure 3-1. This technology allowed us to achieve our goals and, for the Knudsen number requirement, channels with nominal depths of 0.75 μm and 1.33 μm were fabricated. The channel widths were nominally 50 μm so the aspect ratio was therefore about 65 and 37, respectively. Sumps were incorporated at the inlet and outlet of the channel for the on-chip pressure measurement requirement and they are discussed below. The lengths of the channels fabricated in this work were 5 mm, 7.5 mm and 10 mm.

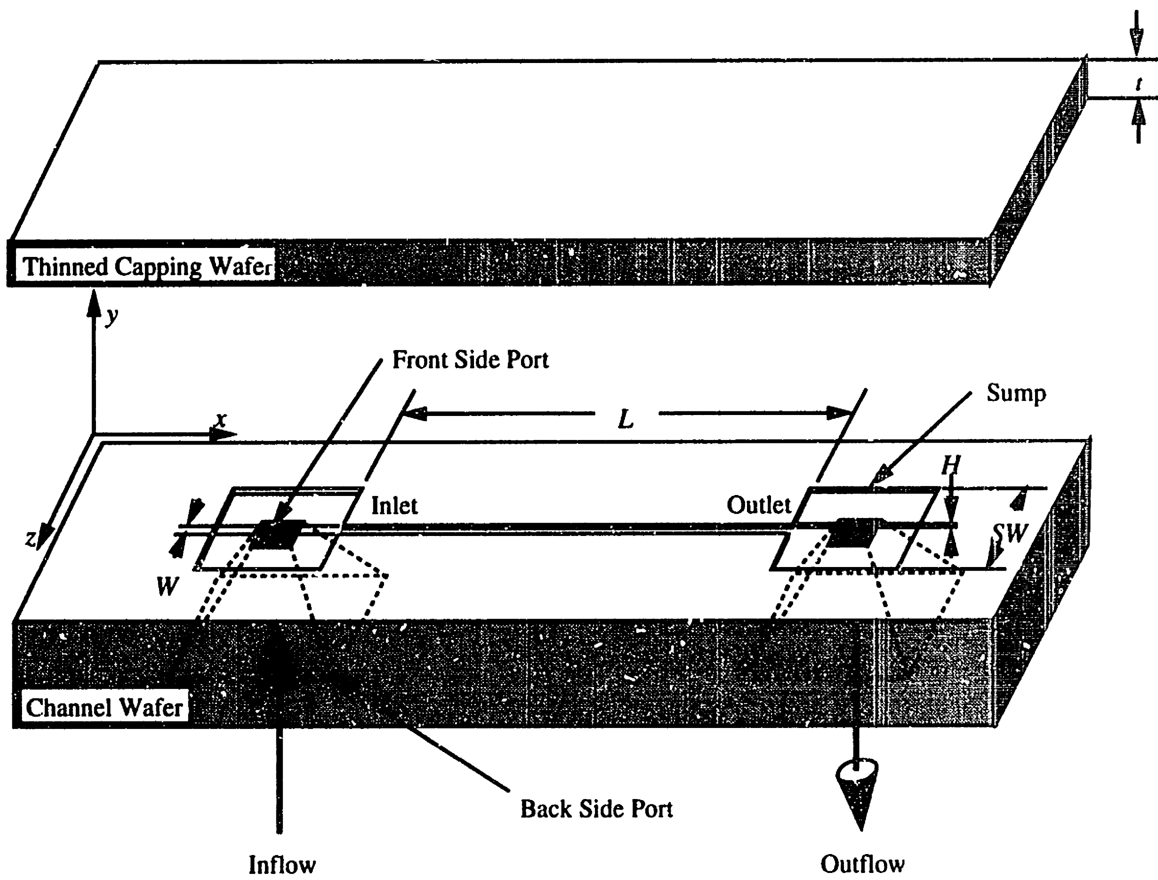

Figure 3-1: Exploded view of a typical micromachined channel

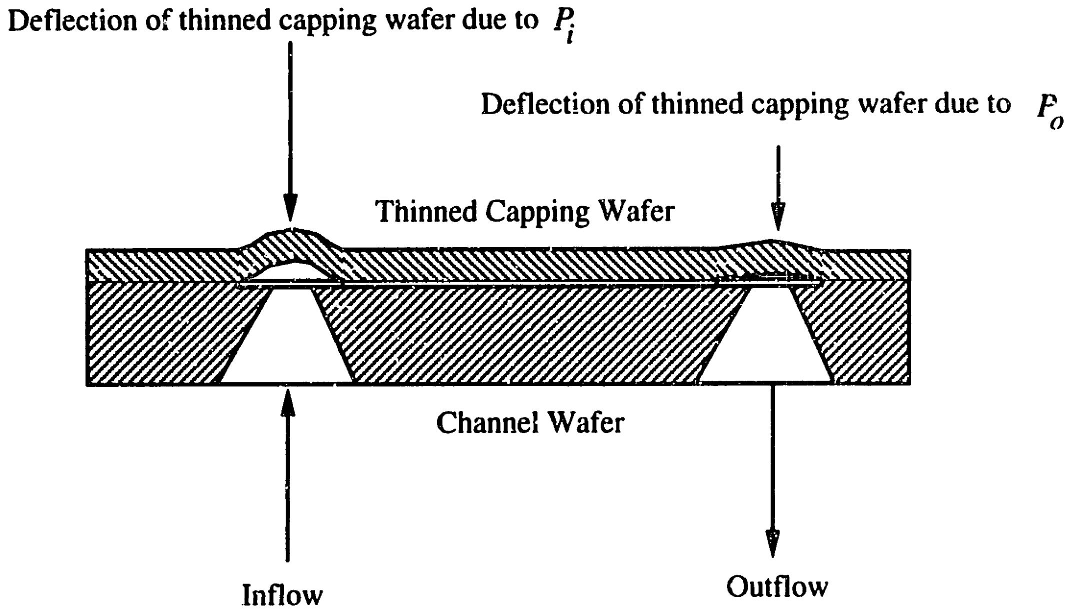

Figure 3-2: Cross sectional view of capping wafer deflection

3.1.1 Sumps

In an attempt to define an appropriate on-chip pressure measurement technique, the microchannels were designed such that there exists an inlet and outlet reservoir or sump (see Figure 3-1). It is assumed that the pressures within these sumps are uniform and equal to the inlet and outlet pressures. These pressures will cause a deflection of the capping wafer over the sumps (sump diaphragm), that is functionally dependent upon the geometry of the sump and the capping wafer thickness (see Figure 3-2).

Disregarding the effect of the channel inlet on the boundary condition around the perimeter of the sump, the functional relationship for the deflection of the capping wafer over the sump is given by [12]:

$$\Delta_{max} = 0.0499 \frac{(P_{appl} - P_{atm}) S W^4}{E t^3} (1 - \nu^2), \tag{3.1}$$

where

P_{appl} = applied absolute pressure,

P_{atm} = atmospheric pressure,

SW = sump width (see Figure 3-1),

E = Young's modulus of silicon,

t = thinned capping wafer thickness (see Figure 3-1),

ν = Poison's ratio.

The characteristic geometric parameter that determines the response of the sump is:

$$0.0499\frac{SW^4}{t^3}.$$

This parameter is constant for any sump geometry and is discussed further in Section 3.5.

For silicon-based pressure sensors, it is the diaphragm deflection measurement of similar structures that determines pressure and there are primarily two ways in which the deflection is transduced: capacitance change and resistance change. In this study, an optical technique for deflection measurement is demonstrated, where the maximum deflection is directly measured and the pressure can be determined by Equation 3.1 (see Section 3.5 for further discussion).

It should be noted that the capping wafer above the channel also tends to deflect when the bonded channel is energized. However, because the channel is only 50 μm wide, the deflection associated with the displacement of the capping wafer over the channel is negligible.

3.1.2 Wafer Layout

The channels are laid out in a 3×3 grid on the channel wafer (see Figure 3-3). Each grid contains 5 similar channels for a total of 45 channels per wafer. Table 3.1 gives the nominal channel characteristics associated with each grid space. See Appendix B for the full mask geometry.

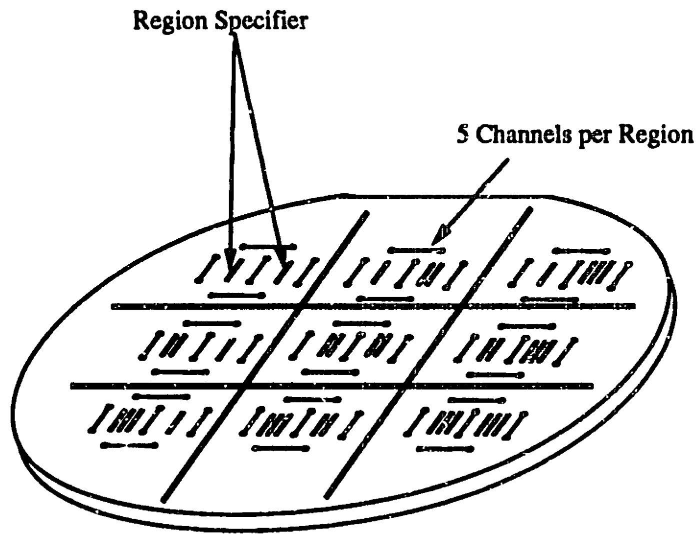

Figure 3-3: The wafer is divided into nine separate regions

REGION	SUMP SIZE(μm)	CHANNEL LENGTH(mm)
I, I	200	5
I, II	400	5
I, III	800	5
II, I	200	7.5
II, II	400	7.5
II, III	800	7.5
III, I	200	10
III, II	400	10
III, III	800	10

Table 3.1: Channel specification of wafer regions

3.2 Channel Fabrication

There are two fabrication techniques carried out in the work of this thesis. Both utilize wafer-bonding technology and, although the fabrication techniques are different, similarities between the two procedures exist. For instance, both fabrication techniques are two mask, two wafer (channel wafer and capping wafer) processes.

To begin microchannel fabrication, both the channel and capping wafer are backside polished in an attempt to insure smooth surfaces which facilitates several processing steps. The back side polishing is done by an outside vendor (Silnet). All subsequent work is undertaken in the Microsystems Technology Laboratory of the Massachusetts Institute of Technology.

3.2.1 Fabrication - Plasma Procedure

The primary features of the plasma fabrication procedure are plasma etched channels and capping wafers of variable thickness. By varying the thickness of the capping wafer, the amount of the capping wafer deflection over the channel, assumed negligible for a 10 μm thick wafer, can be increased and one can study the interaction between the solid and fluid mechanics of the channel. The plasma procedure is represented in Figures 3-4, 3-5 and 3-6 and a complete process traveller is given in appendix A.

Channel Wafer

The processing involved in the fabrication of the channel wafer is represented in Figure 3-4 and progressed as follows. The channel wafer, an <100> n-type prime double-polished .05 to 2 Ω-cm wafer, was oxidized to a nominal thickness of 500 Å. After the oxide growth, the wafer was ion-implanted. The implant is employed on the back side of the channel wafer to facilitate electrical contact, important for Sequence 11 of Figure 3-6, the thinning or etch-back step.

After the implant, the oxide was removed and a photoresist was spun and patterned. The patterned photoresist was used as a mask to the plasma etch, which defines the channel depth. The plasma etch step (Sequence 3 of Figure 3-4) utilized an SF_6 chemistry. The etch rate characteristic of the particular mask used to define

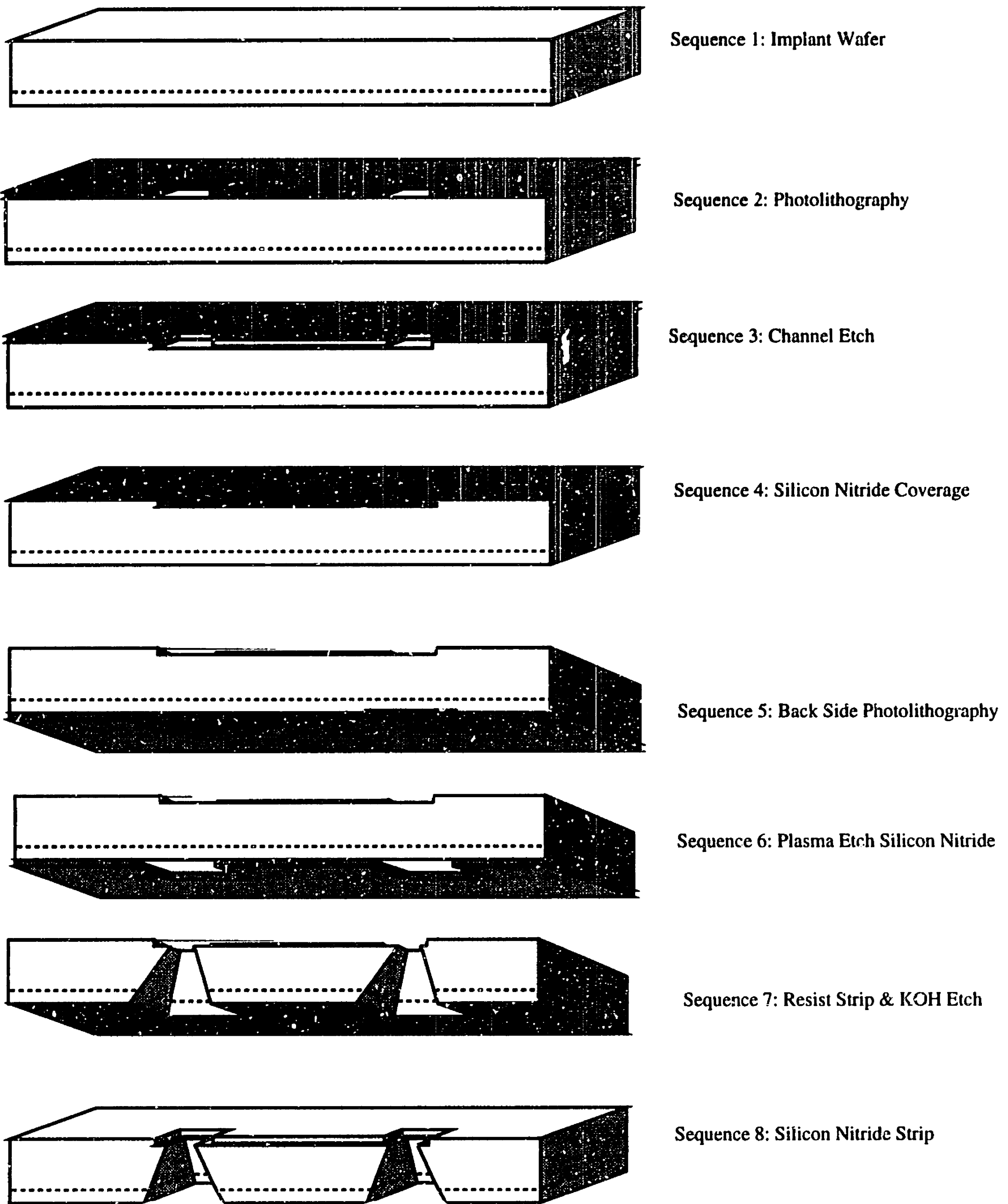

Figure 3-4: Channel wafer fabrication sequence - plasma procedure

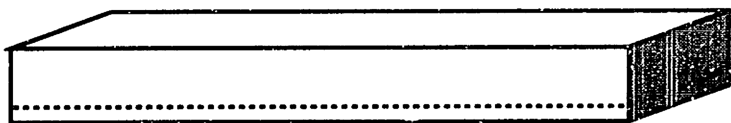

Figure 3-5: Capping wafer fabrication sequence - plasma procedure

the channel geometry was 0.75 μm per minute. With this plasma etch, channels nominally 0.75 μm deep were fabricated.

Next, 1500 Å of silicon nitride was deposited. The silicon nitride was used as a mask for subsequent potassium hydroxide (KOH) etching. After depositing the nitride a photoresist was spun and patterned on the back side of the channel wafer (Sequence 5). The silicon nitride mask was then patterned (Sequence 6). Upon completion of the patterning of the silicon nitride mask, the photoresist was stripped. The wafer was then etched in 20% KOH at 56.5 °C for 29 hours to open the back side ports. The KOH stopped on the silicon nitride of the front side. After the back side port etch, the channel wafer was completed by stripping the silicon nitride mask (Sequence 8).

Capping Wafer

The <100> p-type 10 to 20 Ω-cm double-polished capping wafer used to complete the channel was oxidized and implanted. The implanted dopant was then driven into the wafer with an 8 hour drive-in. This technique establishes a p-n junction at a depth of 10 μm from the surface of the implanted face. This junction defines the thickness of the thinned capping wafer in Sequence 11.

Bonded Channel Wafer

Sequence 10 is the bonding sequence and the step where the channel wafer and the capping wafer come together (see Figure 3-6). The bonding step includes an RCA clean, a contact between the wafers and a post-contact anneal. After contact, the two wafers are inspected for voids under an infrared source. The wafers are then

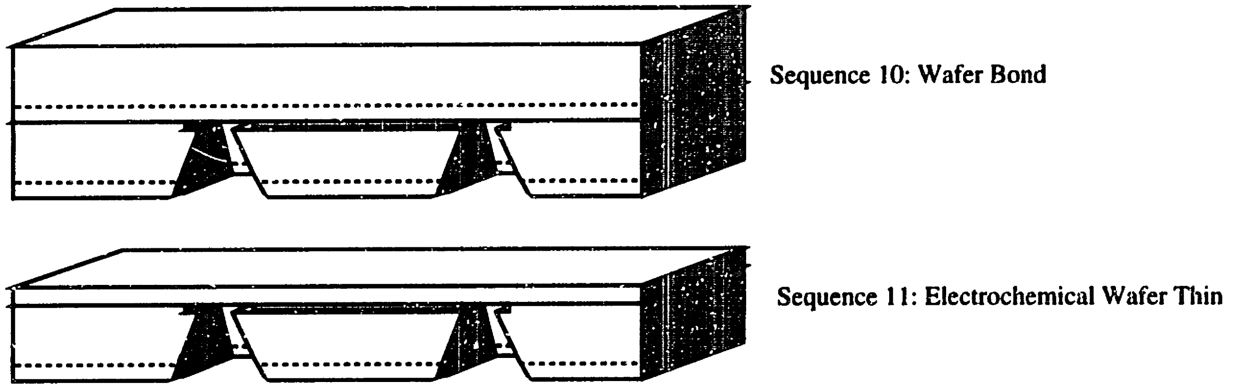

Figure 3-6: Bonded wafer fabrication sequence - plasma procedure

mechanically pressed in an attempt to remove any voids present. The bonding is completed with an anneal in nitrogen at 1000 °C for 70 minutes. This usually helps to remove voids and acts to make the bond permanent. The structure now becomes a bonded channel wafer.

The electrochemical etch step (Sequence 11) was next. In Sequence 11 the capping wafer side of the bonded channel wafer is etched in KOH at 95 °C. A potential is applied across the bonded channel wafer in this sequence and the etch stops at the implanted junction of the capping wafer[13]. At this point the bonded channel wafer of the plasma etch fabrication procedure is complete.

In order to facilitate handling of the channels, the wafer is die sawed into separate chips.

3.2.2 Fabrication Results - Plasma Procedure

Channel Wafer

There are 3 nominal channel lengths: 5 mm, 7.5 mm, and 10 mm. Each channel has a variable length due to photolithographic techniques that is assumed to be $\pm 10\mu m$. The channel width was measured optically with a scaled reticle and the channel depth was measured using a Dektak profilometer. The results are given in

PARAMETER	NOMINAL VALUE(μm)	VARIATION(μm)
length (L)	nominal value	±10
width (w)	50	±0.25
height (H)	0.756	±0.040

Table 3.2: Results from plasma fabrication procedure

Table 3.2

A typical surface profile for the plasma etch fabrication sequence is given in Figure 3-7.

Bonded Channel Wafer

All attempts at thinning the bonded channel structure failed and consequently, the on-chip pressure measurement technique discussed earlier was not fully implemented. The reason for the failure appears to be an incompatibility with the electrochemical hardware[1]. A teflon wafer holding chuck that allows for back side electrical contact, while keeping the back side from KOH, incorporates an o-ring seal and a vacuum mount [14]. After mounting the wafer on the chuck, the back side ports of the wafer induced a stress concentration of sufficient magnitude, to cause the wafer to shatter after several hours of thinning. Upon failure, the wafer began an uncontrolled etch and the dimensional control of the etch stop layer was lost. Although the electrochemical etch failed and the wafer shattered, enough channels survived to demonstrate the feasibility of the deflection pressure measurement technique (see Section 3.5).

3.2.3 Fabrication - Oxide Procedure

In part, because of the poor dimensional control of the plasma etch procedure, a second approach to fabricating micron sized channels was undertaken. This approach is described in Figures 3-8 and 3-9. The main feature of this procedure is that, unlike the plasma etch procedure, the channel is not etched in the silicon of the channel wafer. Instead, an oxide is grown on the prime wafer and the channel is etched in

[1]This problem has since been solved (see Chapter 5).

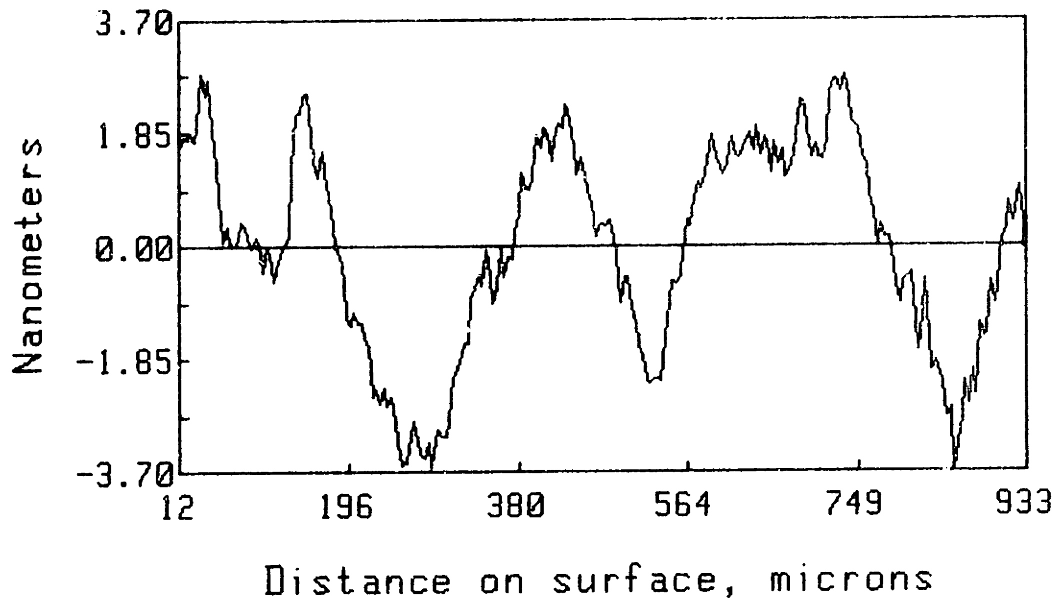

Figure 3-7: Surface profile of channel face - plasma procedure

the oxide. The oxide thickness defines the channel height and is uniform across the wafer. However, this procedure does not allow for thinning of the capping wafer by electrochemical means and precludes the use of the sump deflection as a means to measure the inlet and outlet pressures.

Channel Wafer

As before, the channel wafer is an <100> n-type prime double-polished .05 to 2 Ω-cm wafer. An oxide with a nominal thickness of 1.33 μm was grown on the wafer (Sequence 1 of Figure 3-8). The oxide was then patterned and etched in buffered HF. After channel etching, silicon nitride, which is used as a mask for subsequent KOH etching, was deposited on the wafer (Sequence 3). The nitride on the back side was patterned and etched. The back side ports were then etched in KOH at 56.5 °C for 29 hours, the etch stopping on the front side silicon nitride. The final step in processing the channel wafer was a silicon nitride strip (Sequence 7).

Capping Wafer

The capping wafer is an n or p-type <100> double-polished prime wafer of any resistivity that requires no processing; back side polishing is not essential.

Bonded Channel Wafer

Sequence 8 is the bonding sequence and the step where the channel wafer and the capping wafer come together (see Figure 3-9). This step is identical to the bonding process of the plasma-etch procedure. After bonding, these wafers were also diced into chips.

3.2.4 Fabrication Results - Oxide Procedure

Channel Wafer

The same measurement techniques used in characterizing the plasma fabrication procedure are used to determine the results of the oxide fabrication procedure. The results are given in Table 3.3. Due to the uniformity of the oxide coverage, the oxide fabrication procedure yields channels considerably more uniform than the plasma-etch procedure. There is a suspicion, however, that the height of the channel was improperly characterized (see Section 4.5).

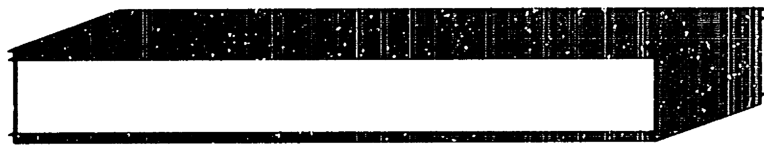

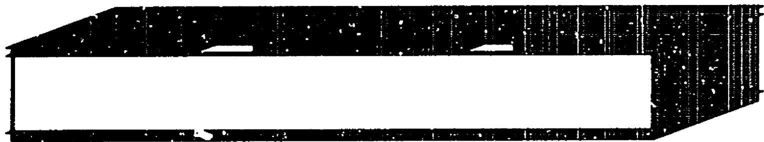

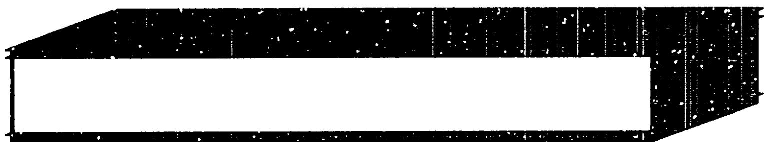

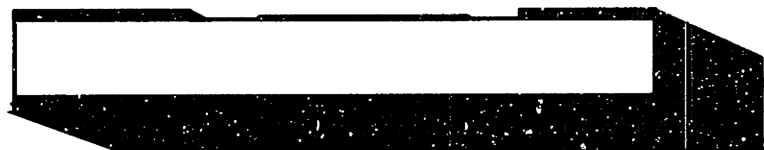

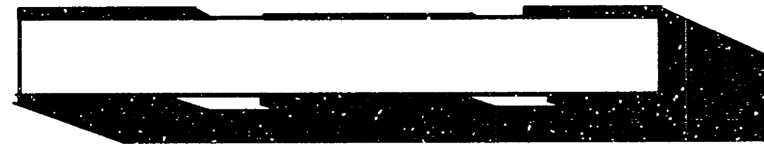

Figure 3-8: Channel wafer fabrication sequence - oxide procedure

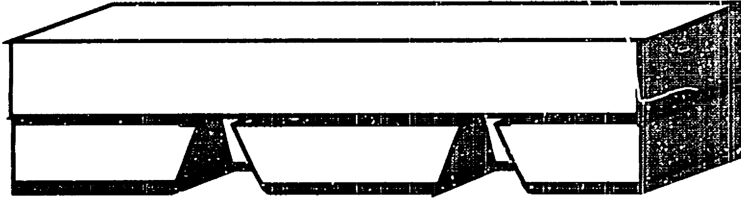

Figure 3-9: Bonded wafer fabrication sequence - oxide procedure

PARAMETER	NOMINAL VALUE(μm)	VARIATION(μm)
length (L)	nominal value	± 10
width (w)	52.25	± 0.25
height (H)	1.33	± 0.01

Table 3.3: Results from oxide fabrication procedure

A typical surface profile of the channel for the oxide fabrication procedure is given in Figure 3-10. The rms roughness for the oxide procedure is about 1/2 as large as the roughness for the plasma procedure.

3.3 Mounting Hardware

Before flow testing could be undertaken, a method had to be devised to couple the channel with the instrumentation used to measure the flow characteristics. Because the pressure drop through the channels can typically be on the order of tens of atmospheres, an interfacial seal must be made between the instrumentation and the microchannel chip that holds its integrity to these pressures.

The approach initially undertaken in this work was designed to allow for the chip to be mounted on a rigid plate or manifold. The manifold, with the mounted chip, was then to be attached to the piping system via a pressure chuck (see Figure 3-11). There are o-ring seals between the pressure chuck and manifold, while the seal between the microchannel chip and manifold was to be maintained with an adhesive-

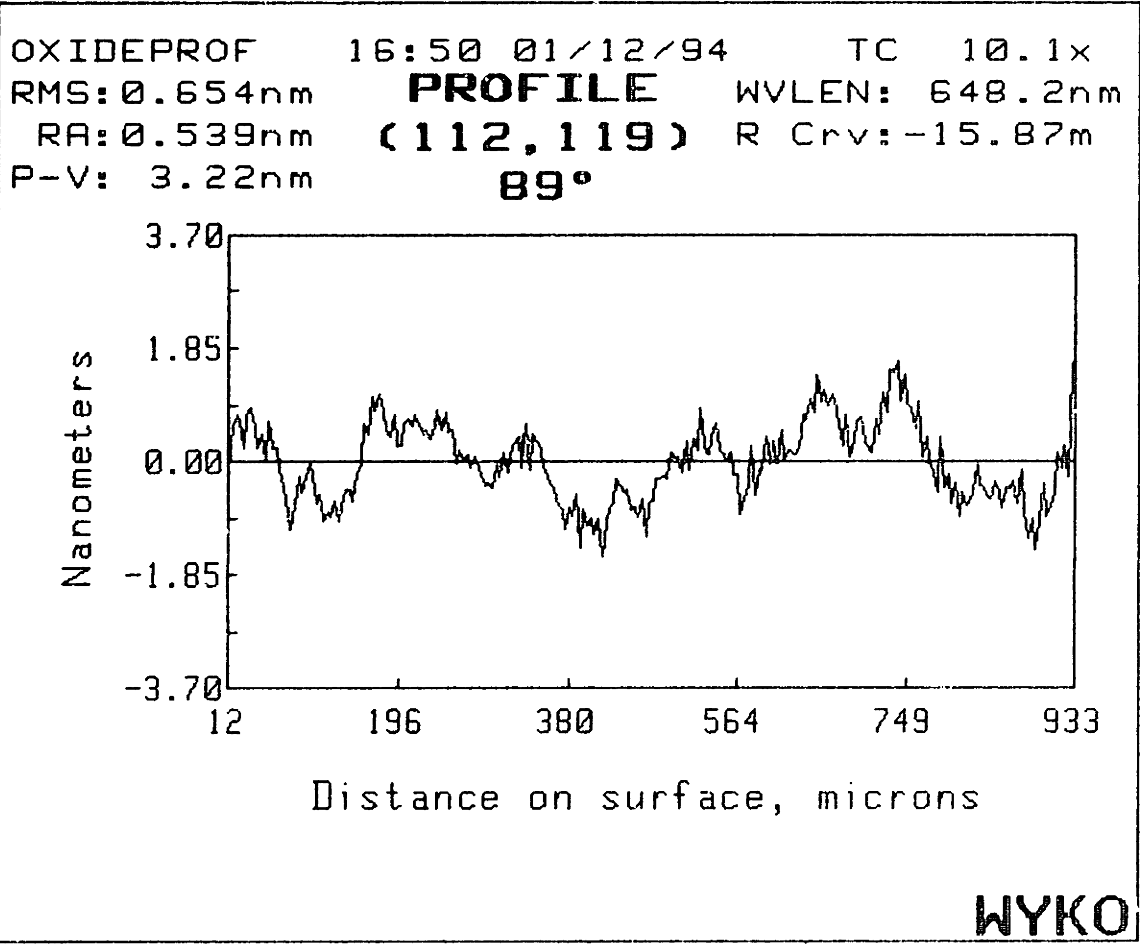

Figure 3-10: Surface profile of channel face - oxide procedure

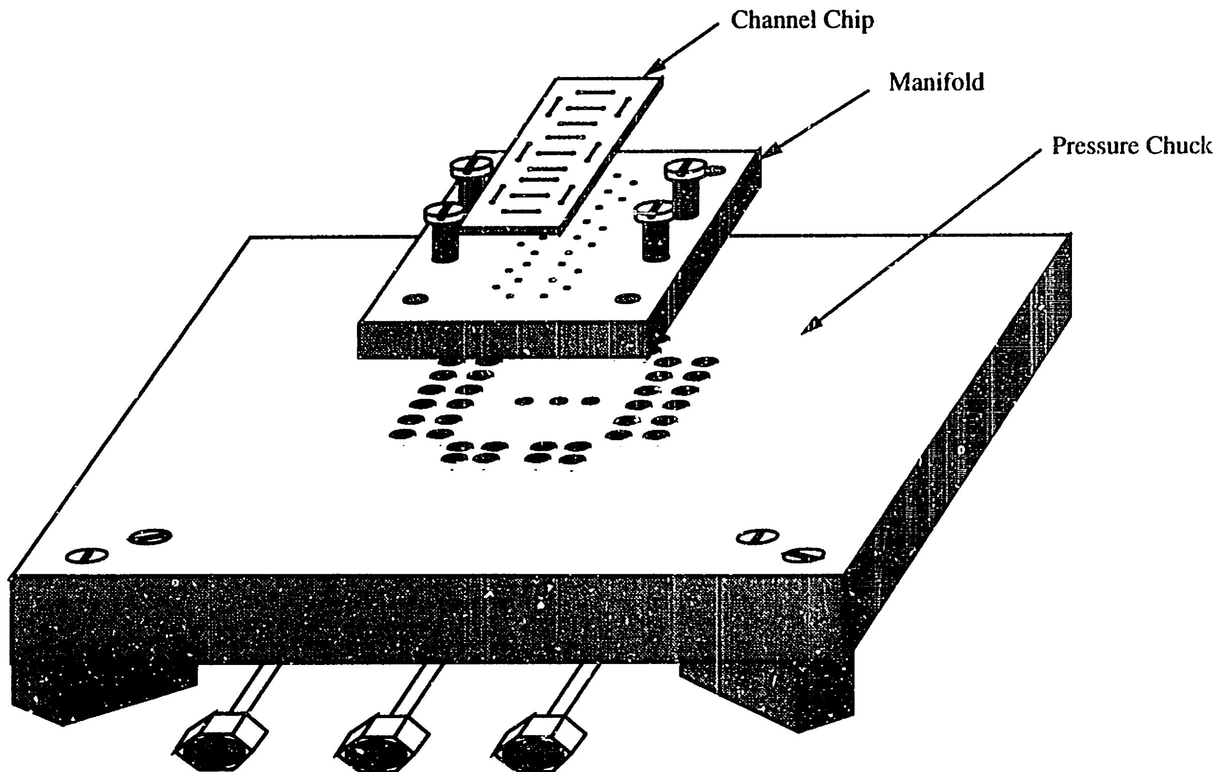

Figure 3-11: Exploded view of initial wafer chip and mounting hardware

sealant. In this way, the position of the manifold, with respect to the pressure chuck, was to determine which channel got energized. This method of mounting would have allowed access to the surface of the bonded channel wafer and thus would have provided the ability to measure the deflection of the capping wafer over the sumps[2]. However, because the electrochemical thinning was unsuccessful, it was no longer necessary to have access to the thinned side of the bonded channel wafer. Without this requirement, the need to solve the adhesive-sealant application problem was negated. Instead of mounting the chip onto the pressure manifold, the chip was mated directly to the o-rings of the pressure chuck by mechanical clamping (see Figure 3-12).

[2]In fact, this method *is* used in the pressure measurement method discussed in Section 3.5

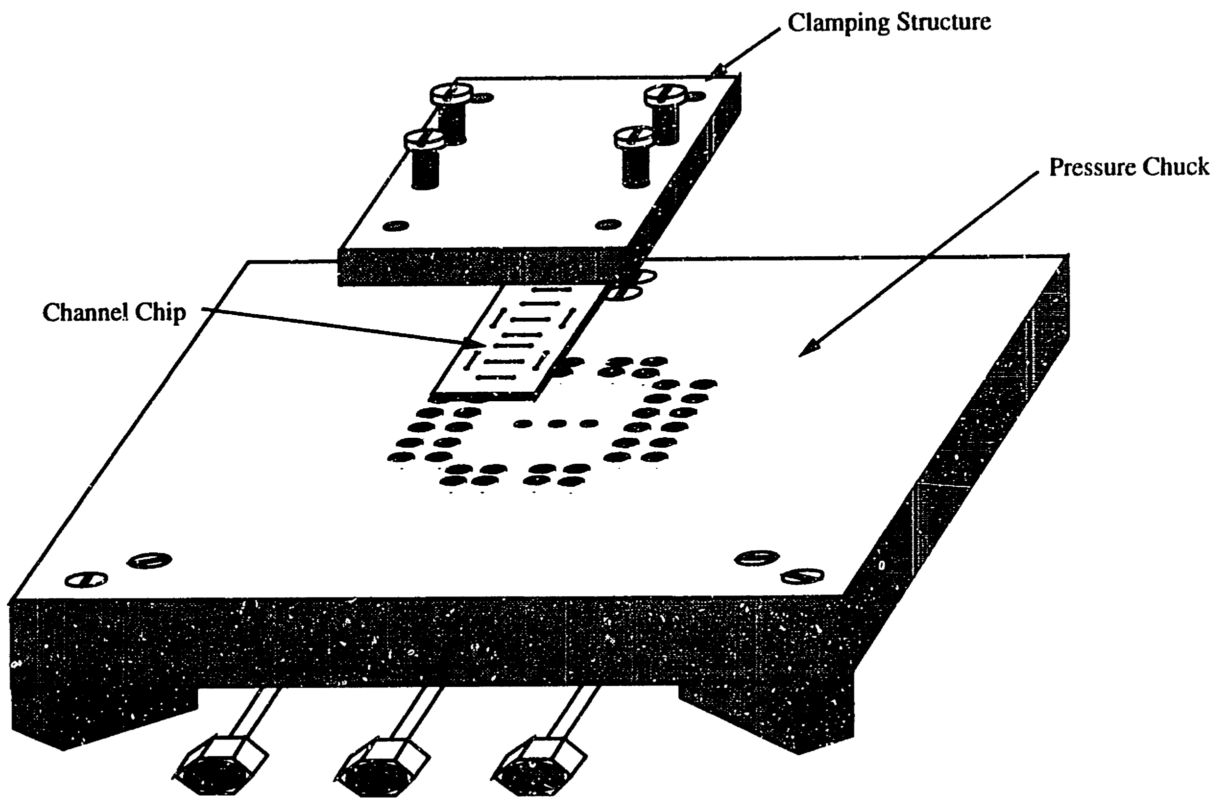

Figure 3-12: Exploded view of final wafer chip and mounting hardware

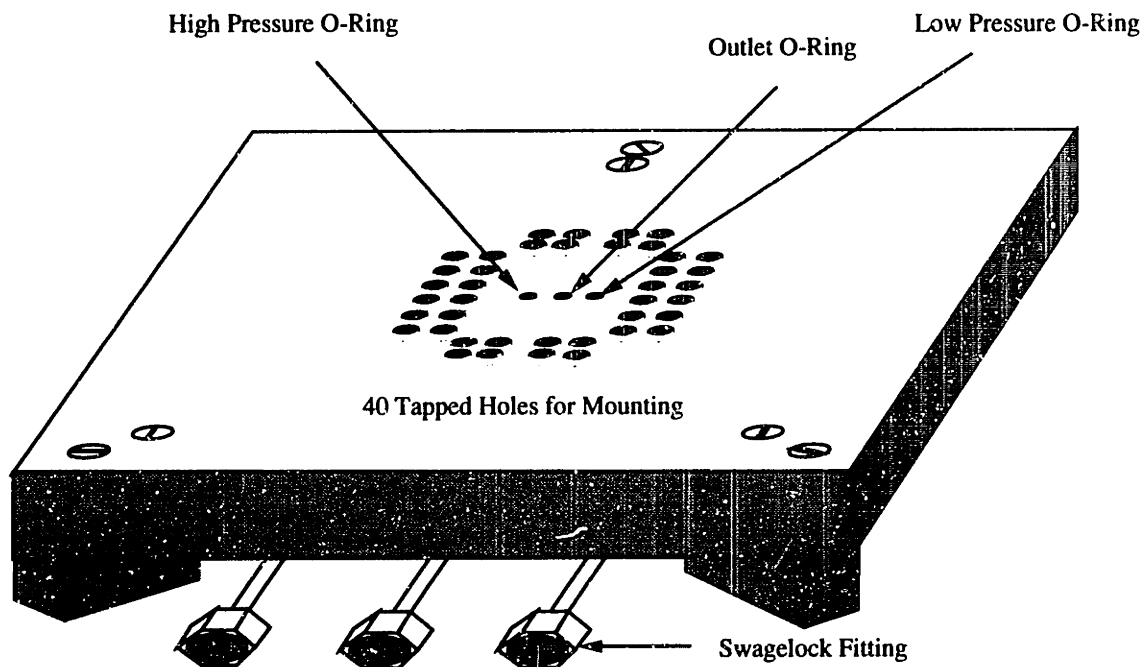

Figure 3-13: Features of the pressure chuck

3.3.1 Pressure Chuck

The stainless steel pressure chuck was designed with three o-rings and associated holes for fluid flow (see Figure 3-13). The middle hole is for the channel exhaust and was designed for an o-ring application at or below atmospheric pressure. On both sides of the central exhaust hole are inlet holes. One of the inlet holes, and the associated o-ring, is for channel inlets at or above atmospheric pressure. The other hole and o-ring was designed for channel inlets at or below atmospheric pressure.

3.4 Mass Flow Measurement

The flow rates associated with microchannel flows are such that commercially available flow meters are insufficient to resolve them. Sensitive flow sensors available presently can resolve flows on the order of 10^{-1} SCCM[15]. A mass flow expected in typical channels of this study is on the order of ng per second. This corresponds to about 10^{-4} SCCM for room-temperature nitrogen; well below the resolution of commercial sensors. Therefore, a method had to be devised that allowed for the measurement of these small flow rates.

By measuring the pressure drop of a charged tank that is upstream of the channel and draining through the channel, one can achieve mass flow measurements of sufficient order.

Assuming ideal gas behavior, the mass within a system of known volume is given by:

$$m_s = \frac{P_s V_s}{R T_s}, \tag{3.2}$$

where

$$\begin{aligned} m_s &= \text{mass within system,} \\ P_s &= \text{pressure within system,} \\ V_s &= \text{volume of the system,} \\ T_s &= \text{temperature of system.} \end{aligned}$$

As the system is drained and the volume remains constant, the mass flow from the system is given by:

$$\dot{m}_s = -\frac{V_s}{R T_s}\frac{dP_s}{dt} + \frac{P_s V_s}{R T_s^2}\frac{dT_s}{dt}. \tag{3.3}$$

Or, we can write:

$$-\frac{V_s}{R T_s}\frac{dP_s}{dt} = \dot{m}_s - \frac{P_s V_s}{R T_s^2}\frac{dT_s}{dt}. \tag{3.4}$$

If room temperature nitrogen is used as the working fluid and the initial pressure within a 100 cc system is 304 kPa (3 atmospheres), for a desired measurable flow rate of 100×10^{-9} g/s, the drift in temperature of the gas, assumed equal to the temperature of the system, must be less than 8.5×10^{-5} K/s.

In order to reduce this temperature sensitivity, a modified mass flow measurement technique was devised. Instead of measuring the temperature and drop in the absolute pressure of a single system, the mass flow was determined by measuring the time-dependent differential pressure between two similar tanks as one (system tank) was drained through the channel, while the other (reference tank) remained sealed. The advantage of this approach is that, if the reference tank and the system tank have matched thermal masses and are thermally coupled, the system will exhibit common thermal-mode rejection and relieve the thermal sensitivity. By using this technique, the piping system, as well as any pressure sensors, contribute to the thermal masses of the system and reference volumes, thus becoming an integral part of the the mass flow meter (see Figure 3-14). Because of this, the platform, with the exception of the data acquisition hardware, is completely housed in thick Styrofoam; the valves are remotely actuated. The Styrofoam insulation is used to isolate the entire system from the ambient, where thermal fluctuations can be large. Further thermal coupling between the reference and system tanks, where the largest amount of gas resides, is achieved by packing them together in thermal grease.

The system mass is given by Equation 3.2. The reference mass is given by a similar expression. The mass flow from the reference volume is given by:

$$\dot{m}_r = -\frac{V_r}{RT_r}\frac{dP_r}{dt} + \frac{P_r V_r}{RT_r^2}\frac{dT_r}{dt} = 0, \tag{3.5}$$

or

$$\frac{V_r}{RT_r}\frac{dP_r}{dt} = \frac{P_r V_r}{RT_r^2}\frac{dT_r}{dt}. \tag{3.6}$$

Where the subscripts denote the reference properties. Because the mass flow into, or out of the reference tank is zero, the variations in temperature of the reference volume result in a change of pressure of the reference volume. By adding Equations 3.4 and 3.6 we get:

$$\frac{V_r}{RT_r}\frac{dP_r}{dt} - \frac{V_s}{RT_s}\frac{dP_s}{dt} = \dot{m}_s + \frac{P_r V_r}{RT_r^2}\frac{dT_r}{dt} - \frac{P_s V_s}{RT_s^2}\frac{dT_s}{dt}. \tag{3.7}$$

If the reference and system volumes possess similar thermal masses and are ther-

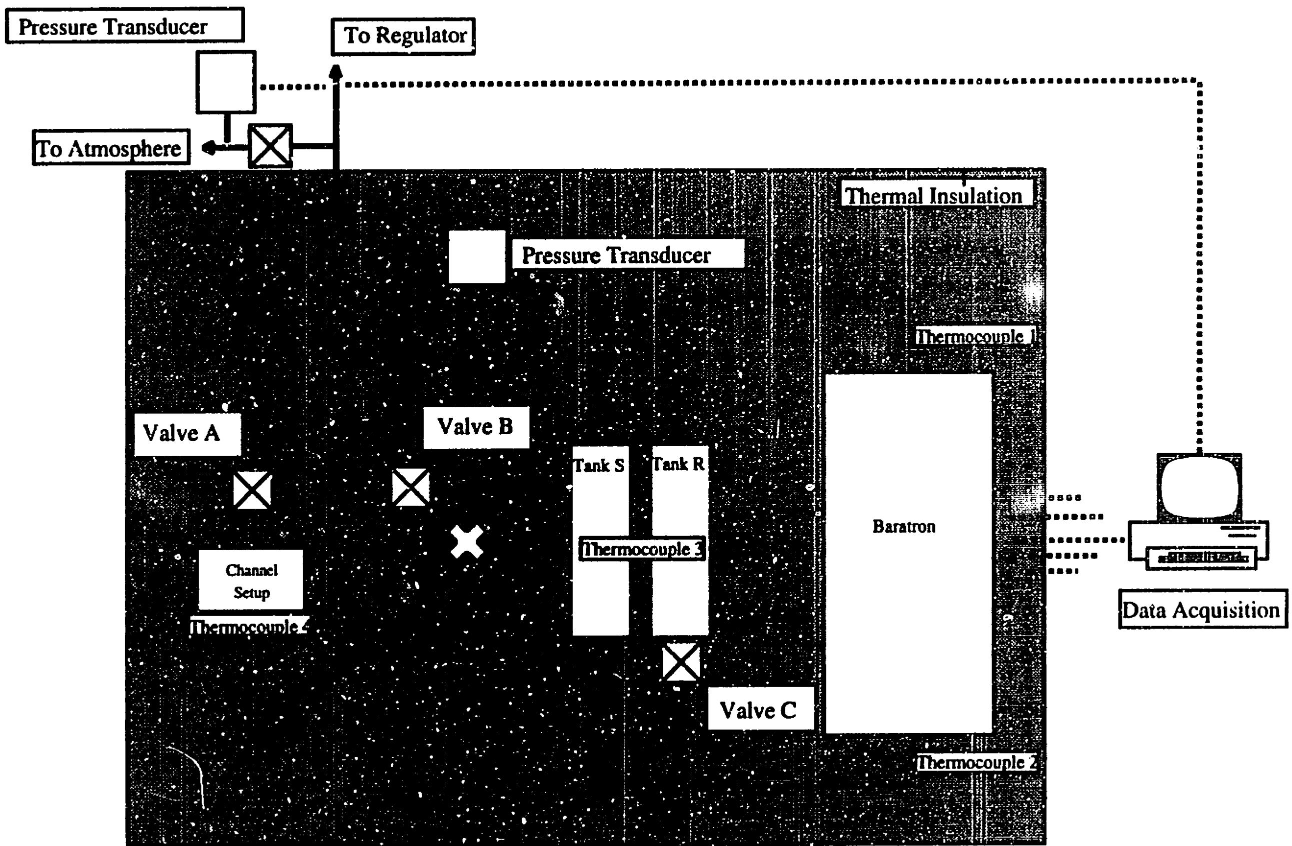

Figure 3-14: Test platform

mally coupled, we can say:

$$T_s = T_r$$

and

$$\frac{dT_s}{dt} = \frac{dT_r}{dt}.$$

The mass flow from the system volume can now given by[3]:

$$\dot{m}_s = \frac{V_s}{RT_s}\frac{d(\Delta P)}{dt} - \frac{V_s \Delta P}{RT_s^{\ 2}}\frac{dT_s}{dt}. \tag{3.8}$$

Where,

$$\Delta P \quad = \quad P_r - P_s.$$

For a desired measurable flow rate of $100 \times 10^{-}9$ g/s, the temperature drift for this technique must be less than 8 K/s, an improvement in magnitude of 5 orders. The performance of the mass flow measurement technique is discussed further in Section 4.2

3.5 Pressure Measurement

For the flow data discussed in Chapter 4, the inlet and outlet pressure for flow testing are measured off-chip with pressure transducers (see Figure 3-14). However, the method by which the inlet and outlet pressure of the channel was designed to be measured is an integral feature of the overall channel design and was discussed in Section 3.1.1(see Figure 3-2. The deflection is correlated to the pressure by means of Equation 3.1. The geometry of the sump is controlled by the photolithographic process and the thickness of the capping wafer is controlled by the implant, drive-in and electrochemical etch discussed in Section 3.2.1. Although no complete wafers survived the electrochemical etch, there were enough remnants to complete a deflection study in order to demonstrate the feasibility of utilizing an optical technique for pressure measurement. Because of the shattering of the wafer, any dimensional

[3]The system volume was measured to be 66.8 cc.

control on the thickness of the capping wafer was lost and the exact thickness of the membrane residing over the sump was not known. These structures, though not of sufficient quality for flow testing, were used to demonstrate the feasibility of the optical pressure measurement technique.

3.5.1 Deflection Measurement

In order to measure the deflection of the capping wafer associated with the pressure within the channel, a Wyko surface characterization interferometer is employed. Unlike a stylus profilometer, the Wyko uses interferometric principles to determine the geometric characteristics of the surface. When the Wyko is used, the phase change associated with the interference of the incident and reflected light is analyzed and the surface characteristics are determined. Among the surface characteristics given by the Wyko is the maximum peak-to-valley height of the surface. This distance can be taken as the maximum deflection associated with Equation 3.1.

The Wyko can measure the phase change with 10 bits of resolution, therefore the resolution in the surface height is given by [16]:

$$\Delta Z = \frac{\lambda}{4\pi 1024}, \tag{3.9}$$

where

$$\begin{aligned} \Delta Z &= \text{resolved height}, \\ \lambda &= \text{incident wavelength}. \end{aligned}$$

With 650 nm light, the minimum resolvable height is about 0.5 Å. Ideally, one would like to measure heights at least 2 orders of magnitude greater than the minimum resolvable height. Therefore, the nominal displacement should be at least on the order of 5 nm.

The maximum thickness of the capping wafer after thinning is about 10 μm. However, the dimensional tolerance of this thickness is such that a calibration of the geometric parameter, discussed in Section 3.1.1, is necessary. It should be noted that the effect of the actual boundary condition at the channel inlet also mandates

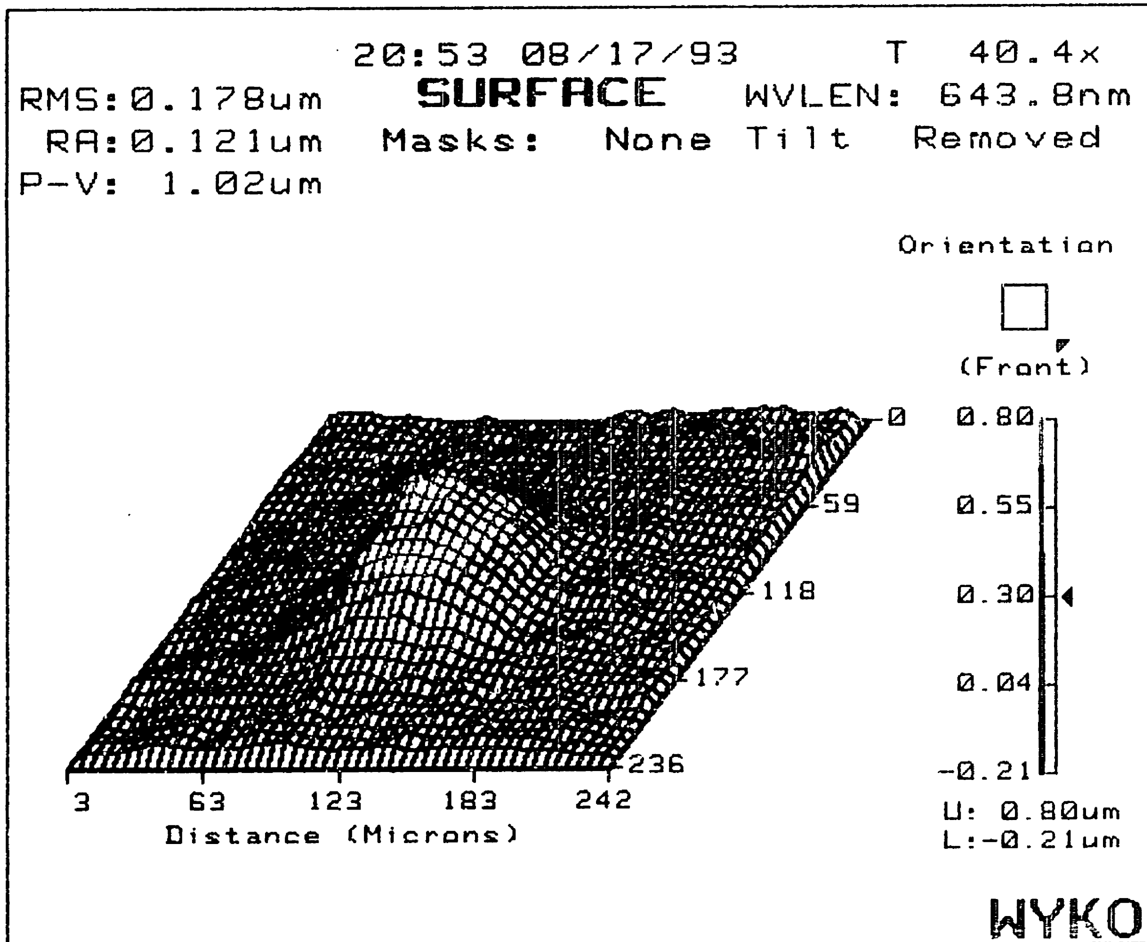

Figure 3-15: Surface deflection of capping wafer at pressure

a calibration of the sumps. In order to calibrate the pressure measuring technique as discussed above, the channels were statically energized. The pressure within the channel structure was increased uniformly over the inlet and outlet. There was no flow through the channel, yet the capping wafer over the sumps deflected. If the pressure is known and the deflection is measured, the geometric parameter, $0.0499\frac{SW^4}{t^3}$, based on the true sump geometry and the thickness of the capping wafer, can be determined. The measurement of the deflection at several static pressures was made. A typical deflection measurement of the 200 μm sump is given in Figure 3-15 and a plot of the deflection as a function of pressure is given in Figure 3-16.

In the small-deflection regime, where Equation 3.1 is valid, the deflection has a linear response to the applied pressure. The slope of the linear region in Figure 3-16

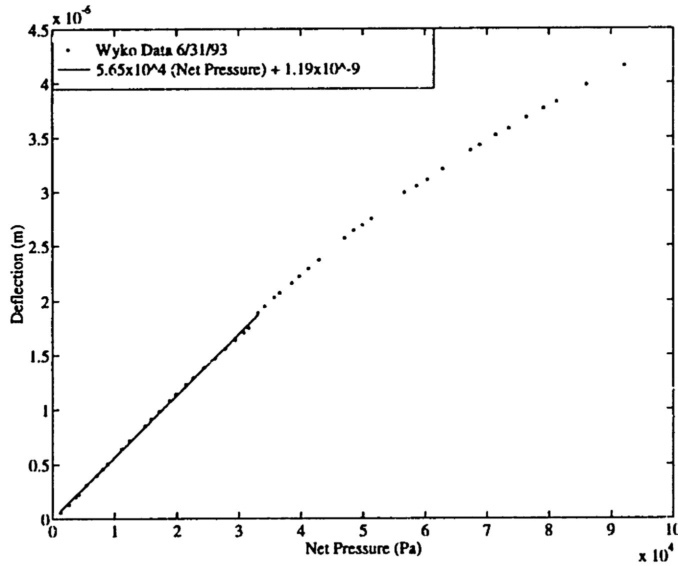

Figure 3-16: Calibration results for sump response

is equal to:

$$0.0499\frac{SW^4}{Et^3}(1-\nu^2), \tag{3.10}$$

where

$$\begin{aligned} SW &= \text{sump width}, \\ E &= \text{Young's modulus}, \\ t &= \text{capping wafer thickness}, \\ \nu &= \text{Poisson's ratio}. \end{aligned}$$

If E is taken as 163 GPa and ν is taken as 0.223, then the geometric parameter of the sump can be determined. The geometric parameter of the sump is:

$$0.0499\frac{SW^4}{t^3} = 5.65 \times 10^{-11}\frac{\text{m}}{\text{Pa}}.$$

Assuming the Wyko can resolve 5 nm displacements, the resolution of this diaphragm pressure sensor is on the order of 28×10^2 Pa.

By using the Wyko, the deflection of the sump diaphragm, and thus, the pressure is easily determined. However, more work is needed to integrate the measurement into a data acquisition system.

Chapter 4

Results and Discussion

Although channels with lengths of 5 mm, 7.5 mm and 10 mm were fabricated in this study, only the channels with nominal lengths of 7.5 mm were used for flow testing. The following data was taken from two separate channels formed by the oxide fabrication procedure. The working fluid was nitrogen and the temperature range for the data is 313 K to 315 K. For all flows the channel outlet was exhausted to atmosphere and the inlet to outlet pressure ratio varied from about 1.2 to 3.

4.1 Physical Parameters

The model presented in Chapter 2 requires several physical parameters and the values of the fluid parameters used in this study are given below in Table 4.1.

The specular reflection coefficient for polycrystalline and crystalline surfaces for

PARAMETER	VALUE
Viscosity (μ) [1]	$18.52 \times 10^{-6} \frac{N \cdot s}{m^2}$
Molecular Diameter (σ) [17]	370×10^{-12}m
Specific Gas Constant (R) [10]	$296.8 \frac{J}{Kg \cdot K}$
Specific Heat Ratio [10]	1.4
Specular Reflection Coefficient	1.0 - 0.3

Table 4.1: Values of physical parameters

a material such as gold is strongly dependent on surface characteristics (surface and absorbed species profiles) [3]. Although no reported values for the specular reflection coefficient of silicon have been found in the literature, a similar dependence is likely. A study of the absorbed species was not undertaken in this work, but the surface profile for a typical channel is given in Section 3.2.4

4.2 Mass Flow Measurements

The mass flow measurement technique discussed in Section 3.4 is based on measuring the time-dependent differential pressure (ΔP) between two tanks as one tank drains through the channel. The time signal for a typical flow experiment is shown in Figure 4-1. Previous to the opening of the valve (demarcated in the figure), the signal has a slight negative slope. This slope can be interpreted in three ways: a leaky reference volume (reference volume with a larger leak than the system volume), a thermal mass mismatch between the system and reference volumes, or a lack of thermal coupling between the system and reference volumes. Since the pressure signal fluctuates both up and down when comparing signals from different tests, we can rule out a leak as the possible cause of this apparent mass flow. Therefore, we believe the most likely explanation of the closed-valve mass flow signal is either a thermal mass mismatch or an incomplete thermal coupling between the reference and system volumes.

Regardless of its origin, the apparent mass flow signal observed when the valve is closed can be subtracted from the open-valve mass flow signal to give a corrected measurement of the flow through the channel. Since the apparent mass flow when the valve is closed is about two orders of magnitude smaller than the mass flow when the valve is open, the correction term is of little significance. This demonstrates that, in relation to the magnitude of the flow rates we wish to measure, the mass flow measurement technique discussed in Section 3.4 is succesful in rejecting thermal signals that would result in spurious mass flows.

Of further note in Figure 4-1, the discontinuity due to the opening of the valve

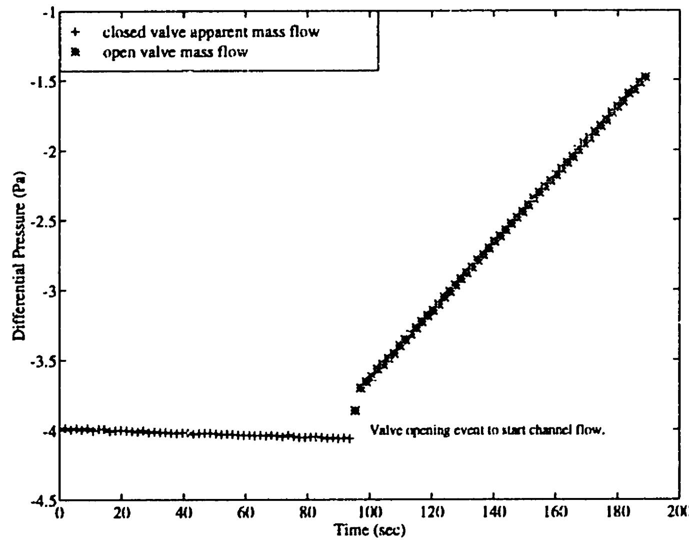

Figure 4-1: Typical differential pressure signal as a function of time for one channel test

can be interpreted as mass injection, which is analogous to charge injection due to the closing of a MOS switch in an electrical circuit.

The measurements described above for determining the mass flow were repeated for various inlet and outlet pressures and the results are shown in Figure 4-2. There was good agreement in the mass flow response of the two channels. Furthermore, it is shown that the mass flow is not a linear function of the pressure ratio; the nonlinearity is due to the compressibility of the gas (see Equation 2.33). Using the mass flow through the channels, one can determine the Mach number and the Reynolds number of the channel flow. The Mach number can be recast in terms of the mass flow:

$$Ma(x) = \frac{\dot{m}\sqrt{RT}}{wHP(x)\sqrt{\gamma}}, \tag{4.1}$$

from which we see that, for a given mass flow, the Mach number is inversely proportional to the pressure along the channel and is maximized at the channel outlet where the pressure is the smallest. For the pressure ratios of 1.2 to 3, the outlet Mach number, Ma_o, ranges from about 100×10^{-6} to 120×10^{-5}.

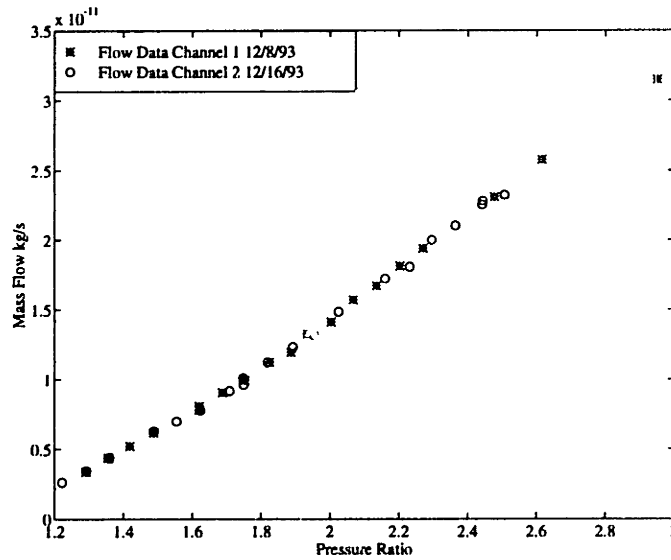

Figure 4-2: Mass flow as a function of pressure ratio

The Reynolds number, based on the channel height, can be shown to be:

$$Re = \frac{\dot{m}}{w\mu}. \tag{4.2}$$

The Reynolds number is a linear function of the mass flow and, for the pressure ratios of this experiment, varied from about 2.5×10^{-3} to 35×10^{-3}.

4.3 Knudsen Number

The Knudsen number is not a function of the mass flow and from Equation 2.4 and Equation 2.11, the Knudsen number, which is used to determine the validity of the continuum assumption, is given by:

$$Kn(x) = \frac{\kappa T}{P(x) H \sigma^2 \pi \sqrt{2}}.$$

The Knudsen number is a function of pressure and therefore is variable along the length of the channel. A plot of the inlet and outlet Knudsen number as a function of pressure ratio is shown in Figure 4-3. The outlet Knudsen number has some variability in the data, which is due to the fluctuations in atmospheric pressure over the course

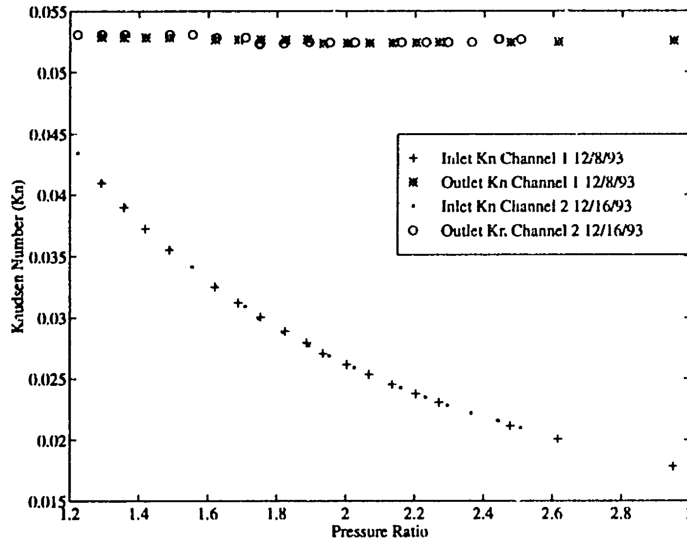

Figure 4-3: Inlet and outlet Knudsen number as a function of pressure ratio

of the experiment.

4.4 Assumption Verification

Several assumptions were fundamental to the analysis discussed in Chapter 2. Among the assumptions made in this analysis was that the flow was incompressible, isothermal, fully developed and two-dimensional.

Using Equations 4.1 and 4.2 and the results of Section 2.3.1, the criterion for incompressible flow can be shown to be:

$$\frac{\dot{m}RT\mu}{wH^2P^2\gamma} \ll 1. \tag{4.3}$$

For the range of parameters used in this study, the constraint on the mass flow for incompressible flow becomes:

$$\dot{m} \ll 7 \times 10^{-3}\frac{\text{g}}{\text{s}}.$$

Clearly this is satisfied. Similarly, by using Equation 4.1 and the results of Sec-

tion 2.3.1, it can be shown that the isothermal flow assumption is valid so long as:

$$\dot{m} \ll \frac{wHP}{\sqrt{RT}}, \tag{4.4}$$

which results in the following constraint:

$$\dot{m} \ll 9 \times 10^{-4} \frac{\mathrm{g}}{\mathrm{s}}.$$

This too is easily satisfied by the present results.

Using the values of w and L from this study and the results of Section 2.3.1, it can be shown that, in order to neglect inlet losses:

$$\dot{m} \ll \mathcal{O}\left(10^{-1} \frac{\mathrm{g}}{\mathrm{s}}\right).$$

The two-dimensional flow assumption is also valid, the aspect ratio of the channels tested is about 37. From Section 2.3.1, the error in the flow rate by assuming two-dimensional flow is less than 0.1%.

4.5 Comparison with Theory

In order to compare the flow results with the models of Chapter 2, the flow data is normalized by the no-slip model and is compared to the slip-flow model normalized by the no-slip model. An expression for the slip-flow model normalized by the no-slip model is given by Equation 2.35, and is repeated below:

$$\frac{\dot{m}}{\dot{m}_{NS}} = 1 + 12 \frac{2 - F}{F} Kn_o P_o \frac{1}{(P_i + P_o)}. \tag{2.35}$$

This expression is linear in the parameter $\frac{1}{(P_i+P_o)}$, with a slope that is a function of F, T and H. For small values of the parameter, $\frac{1}{(P_i+P_o)}$, the solution approaches unity. This implies that for large enough flow rates, the deviation between the slip-flow and no-slip solutions is negligible.

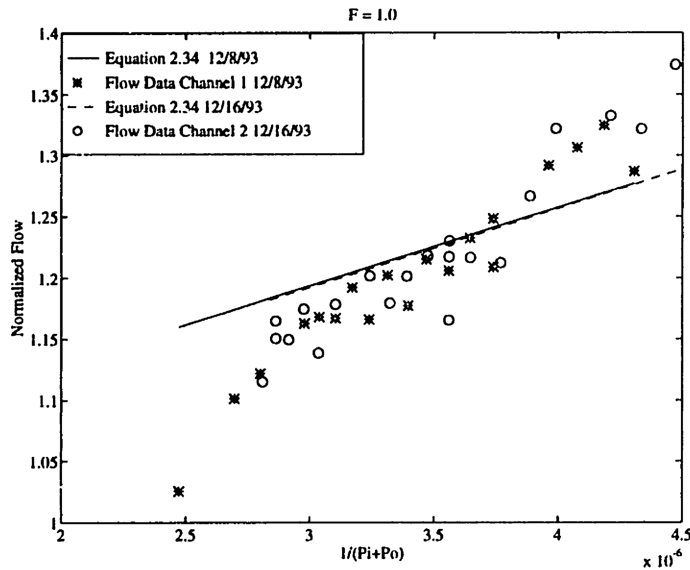

Figure 4-4: A comparison between the flow data normalized by the no-slip solution and Equation 2.35 for $F = 1$

In order to compare the result of Equation 2.35 to the flow data, the flow data is normalized by the solution obtained with the no-slip boundary condition. It can be shown from Equations 3.8 and 2.34 that the flow data normalized by the no-slip solution has the following form:

$$\frac{\dot{m}_{meas}}{\dot{m}_{NS}} = \frac{d\Delta P}{dt}\frac{V_s}{H^3 w}\frac{\mu L}{(P_i + P_o)(P_i - P_o)}, \tag{4.5}$$

where a typical signal for ΔP is given in Figure 4-1. If $\frac{\Delta P}{dt}\frac{1}{P_i - P_o}$ is constant for the mass flow experiments, this expression is linear in the parameter $\frac{1}{(P_i+P_o)}$ and has a slope given by:

$$\frac{d\Delta P}{dt}\frac{V_s}{H^3 w}\frac{\mu L}{(P_i - P_o)}.$$

A comparison is made between the flow data normalized by the solution obtained from the no-slip boundary condition and the result of Equation 2.35 for F= 1, and is shown in Figure 4-4. If the slip-flow model with $F = 1$ accurately described the flow, the data points plotted in Figure 4-4 and the solution of Equation 2.35, also plotted in Figure 4-4, would be colinear. Conversely, if the no-slip model accurately described the flow, the data points would lie along a horizontal line. Although the slip-flow

model, with $F = 1$, does not completely describe the measured flow, it is encouraging that the data is linear in the parameter $\frac{1}{(P_i+P_o)}$. Also, the sign and the magnitude of the slope of the normalized data are consistent with the normalized slip-flow model. Because there is no reason to believe that $F = 1$ for the nitrogen-silicon surface interactions of this study, it is instructive to investigate the impact that different values of F have on the comparison between the model and the measured flow. It can be seen from Equation 2.35 that by altering the value of F, one can change the slope of the normalized slip-flow model. Plots for different values of $1.0 \geq F \geq 0.4$ are given in Figure 4-5.

Although the slope of the normalized slip-flow model can be tailored to fit the slope of the data by altering F, the normalized slip-flow model can not be made to fit the flow data by altering F alone. The normalized slip-flow model has unity as a limit for small values of $\frac{1}{(P_i+P_o)}$. The best-fit line through the normalized data (not shown) has a limit of about 0.7. This indicates that, if the flow data continues along the same trend, the mass flow at large pressure ratios is actually smaller by about 30% than the mass flow given by the no-slip model. This result calls into question, the initial characterization of the microchannel.

It can be seen from Equation 4.5 that the slope of the normalized data has a cubic dependency on the height and a linear dependency on other parameters. To determine the effects that possible errors in the initial characterization of the channel have upon the comparison of the normalized model and the data, it is instructive to see how the data can be made to fit the model.

For large values of $\frac{1}{(P_i+P_o)}$, Equation 2.35 has a limit of unity. If it is accepted that microchannel slip-flow should approach the no-slip model at large values of $\frac{1}{(P_i+P_o)}$ (and the mass flow continues along the same trend), the parameter $\frac{d\Delta P}{dt}\frac{V_t}{H^3 w}\frac{\mu L}{(P_i-P_o)}$ must be increased by about 30%. As well as increasing the limit, altering this parameter also affects the slope of the normalized data. One set of values that can be used to make the normalized data limit have unity as a limit is given in Table 4.2. With these values the normalized model (Equation 2.35) can be made to fit the data, using $F = 0.54$. The results of the curve-fitted data and model are shown in figure 4-6.

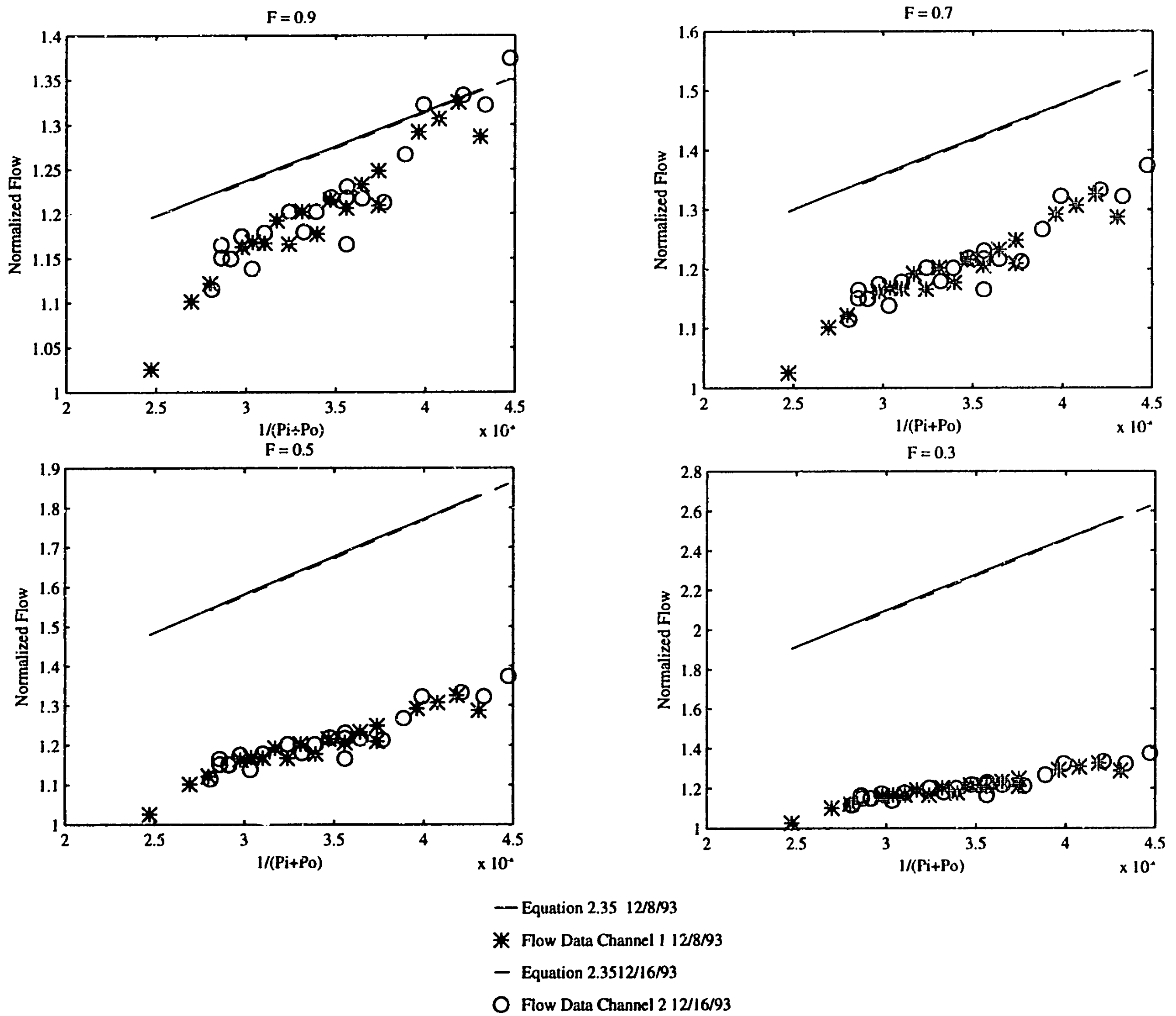

Figure 4-5: A comparison between the flow data normalized by the no-slip solution and Equation 2.35 for various values of F

PARAMETER	VALUE	% ERROR[1]
Height (H)	$1.21\mu m$	-8
Width(w)	$51.25\mu m$	-2
Length(L)	7.5 mm	0
System Volume (V_s)	69.14 cc	+4
Viscosity (μ)	$18.89 \times 10^{-6} \frac{N \cdot s}{m^2}$	+2

Table 4.2: One set of parameters that can be used to model the experimental data

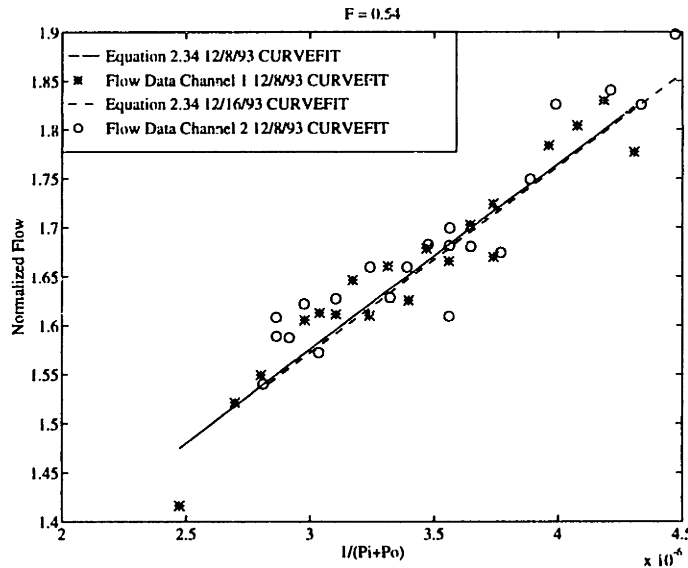

Figure 4-6: A comparison between the flow data normalized by the no-slip solution and Equation 2.35 utilizing the values of Table 4.2 and $F = 0.54$

Though the data can be made to fit the normalized model, Equation 4.5 suggests that there does not exist a simple numerical correction that can be used to remove the slope in the normalized data. This indicates that the flow can not be described by the no-slip solution. However, the values required to make the data fit the slip-flow model are demonstrative of errors significantly larger than the uncertainties reported. Because of this, we can not at the present time accept or reject the slip-flow model. We believe that additional experimentation is required to verify the model.

[1]These values represent % error from the values which were initially assumed to be correct.

Chapter 5

Conclusions

We have shown for microchannel flow that there exists a reduction in the momentum transfer between the working fluid and the channel wall that is functionally dependent on the Knudsen number. This reduction in the momentum transferred from the gas must lead to an increase in mass flow for given pressures and can not be modeled by the no-slip boundary condition solution of the Navier-Stokes equations. Although the model that we derived predicts an increase in the mass flow for given inlet and outlet pressures and possesses the general features of the flow data, it does not accurately model the flow without accepting an initial error in channel characterization. The required error to bring about agreement between the model and the data is larger than the uncertainties reported but we do not see any easy way to re-measure the channel characteristics. Although we can not accept or reject the slip-flow model presented here, we believe it has been shown that, for certain flows that can be achieved in MEMS, the no-slip conditions fails and the specular reflection coefficient, F, is likely less than unity for microchannel flows. Further investigation is required.

We suggest that a more careful channel characterization study be undertaken and that different working fluids be used. Further, features that would allow for pressure measurement along the length of the channel would prove to be a powerful tool in a more detailed study of microchannel flow. By incorporating on-chip pressure taps along the length of the channel (see Figure 5-1) one could compare the pressure distribution for a given mass flow to the prediction of Equation 2.37, and further study

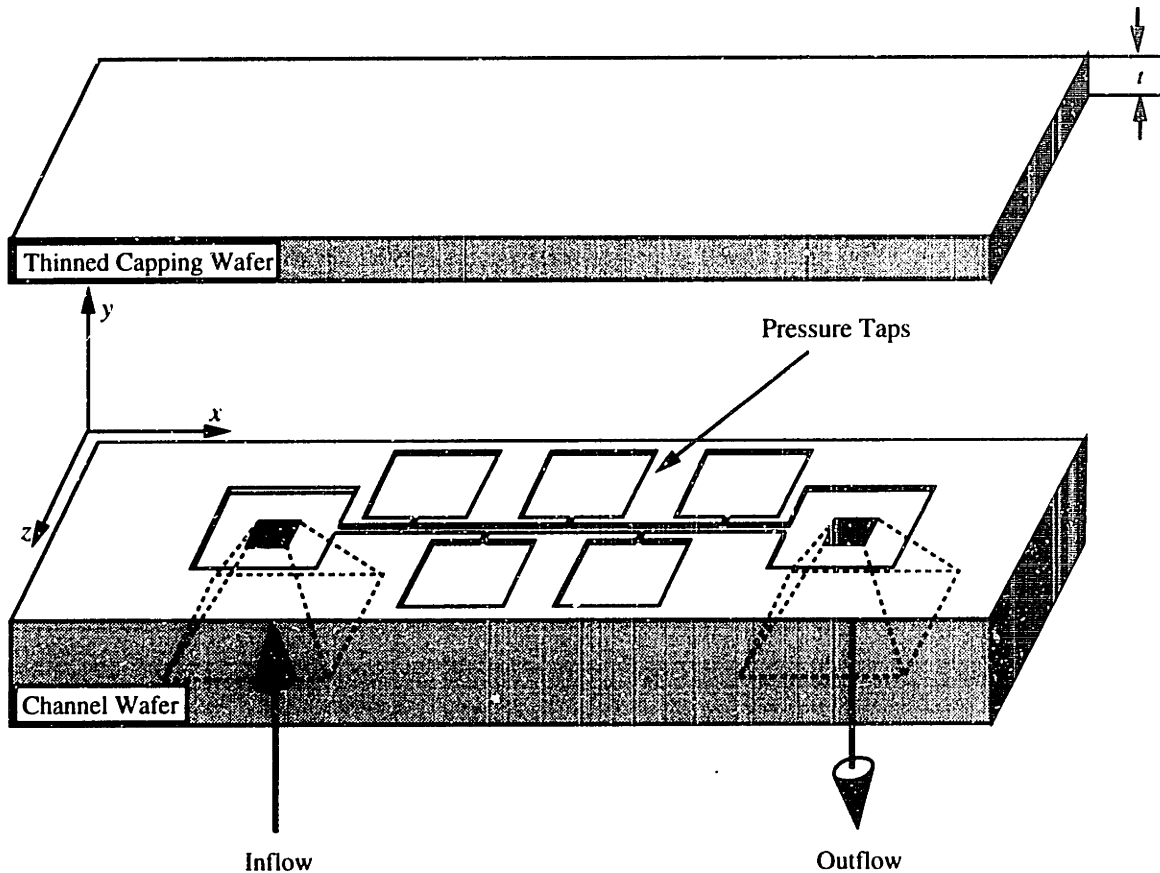

Figure 5-1: To measure the pressure distribution, pressure taps can be included down the length of the channel

the model of Chapter 2. Through a different fabrication technique, this approach is currently being investigated elsewhere [18]. With the present approach, the incorporation of pressure taps along the length of the channel would require us to solve the electrochemical etch problem discussed in Section 3.2.2. By reducing the amount of vacuum applied to the wafer [19], the electrochemical-etch problem has been solved. Although we have demonstrated the feasibility of the optical technique, we believe that the requirement for access to the capping wafer is incompatible with the thermal isolation requirements of the present mass flow measurement technique, but, by using piezoresistive or capacitance transduction, which would require more sophisticated microfabrication, the pressure signal could be transduced.

In addition, we also recommend exhausting the channel exit to sub-atmospheric pressures, which would increase the Knudsen number and, correspondingly, the deviation from the no-slip solution. Also, by exhausting to vacuum, the mass flow would be increased. Another way to increase the mass flow would be to simultaneously test

an array of channels in parallel. For given pressures, the mass flow could easily be increased by an order of magnitude or more. This method, though, would be very sensitive to clogging.

One of the most pleasing results of this work is the development of a sensitive mass flow measurement capability. Presently the magnitude of mass flow required to study the flow in microchannels is on the order of ng per second, small by present-day standards. We have designed a technique that can be used to measure mass flows of this scale which rejects thermal noise. However, the technique does not allow for any dynamic flow measurement, but it could be used as a calibration means for a flow sensor based on viscous loss. This type of sensor would be sensitive and have dynamic capabilities.

Finally, in future studies a means for temperature measurement must be devised.

There are many issues to be resolved, and we believe that continued experimentation on microchannel flow is feasible and will lead to important advances in the fields of microfluids modeling and MEMS.

Appendix A

Process Travelers

PROCESS TRAVELER-PROCEDURE 1

MICROCHANNEL FABRICATION

LOT

LOT OWNER Errol Arkilic

STEP	STEP DESCRIPTION	STATUS	
CHANNEL WAFER			
Starting material : double polished n-type <100> .5-2Ωcm			
1	Stress Relief Oxide	Number wafers	________
	dsro430.set	Opset start	________
	(ICL)	Opset finish	________
2	Implant phosphorus	Number wafers	________
	instop.set (ICL)	Opset start	________
	energy=160keV, dose=5E15 (ICL)	Opset finish	________

3	Channel Photolithography	Number wafers	________
	Mask 1	Opset start	________
	(TRL)	Opset finish	________
4	Plasma Etch Channels	Number wafers	________
	recipe 19	Opset start	________
	1 minute (ICL)	Opset finish	________
5	Photoresist Strip	Number wafers	________
	Pirhana	Opset start	________
	10 minutes(ICL)	Opset finish	________
6	Silicon Nitride Coverage	Number wafers	________
	(ICL)	Opset start	________
		Opset finish	________
7	Port Photolithography	Number wafers	________
	Mask 2	Opset start	________
	(TRL)	Opset finish	________
8	Plasma Etch Port Openings	Number wafers	________
	recipe 13	Opset start	________
	45 seconds (ICL)	Opset finish	________
9	Photoresist strip	Number wafers	________
	pirhana	Opset start	________
	10 minutes (ICL)	Opset finish	________
10	KOH etch	Number wafers	________
	20 % KOH, 56 °C	Opset start	________

	28 hrs (RGL)	Opset finish	________
11	Post KOH clean	Number wafers	________
	(RGL)	Opset start	________
	(TRL)	Opset finish	________

CAPPING WAFER

Starting material : double polished p-type <100> 10-20Ωcm

1	Stress Relief Oxide	Number wafers	________
	dsro430.set	Opset start	________
	(ICL)	Opset finish	________
2	Implant phosphorus	Number wafers	________
	instop.set	Opset start	________
	energy=160keV,dose=5E15(ICL)	Opset finish	________
3	Drive-in	Number wafers	________
	dphosdrive.set	Opset start	________
	recipe 253 (ICL)	Opset finish	________
4	Oxide strip	Number wafers	________
	wsro430.set	Opset start	________
	(ICL)	Opset finish	________

BONDED CHANNEL WAFER

Starting material : Channel Wafer & Capping Wafer

1	Bond Wafers	Number wafers	________
	dbonding.set	Opset start	________

	(TRL)	Opset finish	________
2	Electrochemical Etch	Number wafers	________
	wetetch.set	Opset start	________
	20% KOH 90C (RGL)	Opset finish	________

END

PROCESS TRAVELER-PROCEDURE 2

MICROCHANNEL FABRICATION

LOT

LOT OWNER Errol Arkilic

STEP	STEP DESCRIPTION	STATUS	

CHANNEL WAFER

Starting material : double polished n-type <100> .5-2Ωcm

1	Oxidation	Number wafers	________
	dox13.3k.set	Opset start	________
	(ICL)	Opset finish	________

2	Photolithography	Number wafers	________
	Mask 1	Opset start	________
	(TRL)	Opset finish	________
3	Patern Oxide	Number wafers	________
	wox13.3k.set	Opset start	________
	(TRL)	Opset finish	________
4	Photoresist Strip	Number wafers	________
	Pirhana	Opset start	________
	10 minutes (ICL)	Opset finish	________
5	Silicon Nitride Coverage	Number wafers	________
	(ICL)	Opset start	________
		Opset finish	________
6	Back Side Photolithography	Number wafers	________
	Mask 2	Opset start	________
	(TRL)	Opset finish	________
7	Plamsa Etch Port Openings	Number wafers	________
	recipe 13	Opset start	________
	45 seconds (ICL)	Opset finish	________
8	Photoresist Strip	Number wafers	________
	Pirhana	Opset start	________
	10 minutes (ICL)	Opset finish	________
9	KOH etch	Number wafers	________
	20 % KOH, 56 °C	Opset start	________

	28 Hrs (RGL)	Opset finish	________
10	Post KOH clean	Number wafers	________
	(RGL)	Opset start	________
	(TRL)	Opset finish	________

CAPPING WAFER

Starting material : double polished p-type <100> 10-20Ωcm

BONDED CHANNEL WAFER

Starting material : Channel Wafer & Capping Wafer

1	Bond Wafers	Number wafers	________
	(dbonding.set)	Opset start	________
	(ICL)	Opset finish	________

END

Appendix B

Masks

The process involved in the building of the microchannels is a two wafer two mask sequence. A third mask, developed for this project is not implemented. The third mask is designed for fabricating structures on the thinned capping wafer for identification purposes. Even at 10 microns the thinned capping wafer is opaque, and therefore the structure of the channels on the channel wafer is not visible.

B.1 Mask 1

The first mask is designed to define the planer geometry of the channels. Notice the 3×3 layout of the channels. The characteristics of the channels are given in section 3.1.2. Residing on mask 1 there are some structures not talked about in this thesis. They are designed primarily for test application and are not used in this study.

B.2 Mask 2

The second mask is used to define the back side ports of the channel wafer.

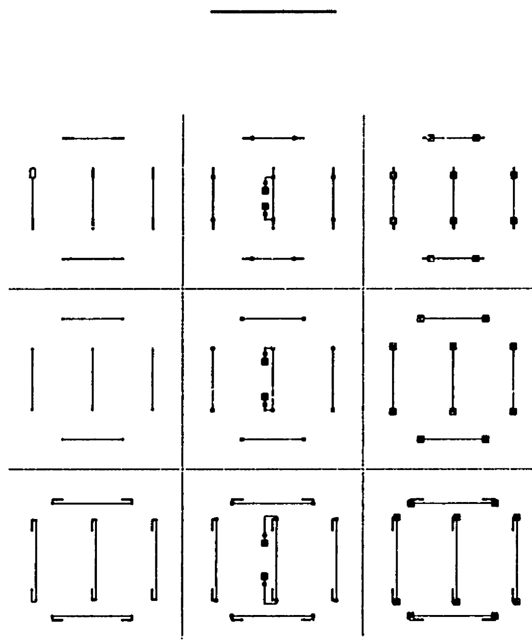

Figure B-1: Mask 1 used to define channel geometry

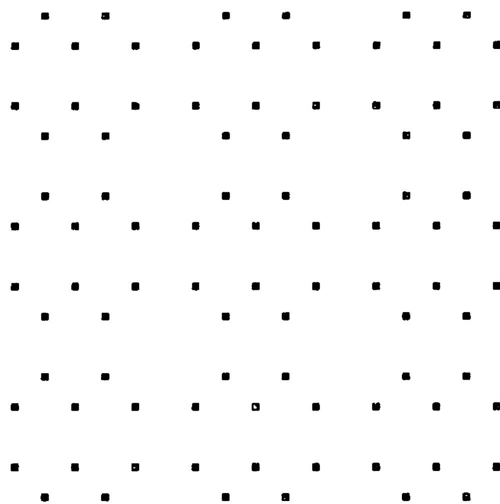

Figure B-2: Mask 2 used to define the back side ports

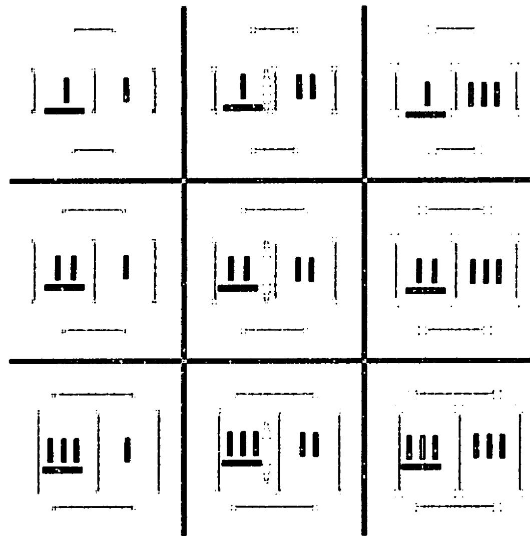

Figure B-3: Mask 3 designed for identification marks

B.3 Mask 3

The third mask is designed to fabricate identification marks on the thinned capping wafer. It is not implemented in this study.

Bibliography

[1] Frank M. White. *Viscous Fluid Flow.* McGraw-Hill, Inc, New York, New York, 1991.

[2] J. Pfahler, J. Harley, Bau H., and J. Zemal. Gas and liquid flow in small channels. In *Micromechanical Sensors, Actuators, and Systems, ASME Winter Annual meeting*, pages 49–59, Atlanta, GA, December 1991.

[3] E. Steinheil, M. Scherber, and M. Seidl. Investigations on the interaction of gases and well-defined solid surfaces with respect to possibilities for reduction of aerodynamic friction and aerothermal heating. In J. Potter, editor, *Rarefied Gas Dynamics.* American Institute of Aeronautics and Astronautics, 1977.

[4] S.A. Schaff and P.L. Chambre. Flow of rarefied gases. In *Fundamentals of Gas Dynamics*, chapter H. Princeton University Press, New Jersey, 1958.

[5] R.G. Lord. Tangential momentum accommodation coefficients of rare gases on polycrystalline metal surfaces. In J. Potter, editor, *Rarefied Gas Dynamics.* American Institute of Aeronautics and Astronautics, New York, New York, 1977.

[6] Warren M. Rohsenow and Harry Choi. *Heat, Mass, and Momentum Transfer.* Prentice-Hall, Inc, Englewood Cliffs, New Jersey, 1961.

[7] Earle H. Kennard. *Kinetic Theory of Gases, With an Introduction to Statistical Mechanics.* McGraw-Hill Book Company, Inc., New York, New York, 1938.

[8] Sir James' Jeans. *An Introduction to the Kinetic Theory of Gases.* Cambridge University Press, London,England, 1962.

[9] D.J. Tritton. *Physical Fluid Dynamics.* Oxford University Press, New York, New York, 1988.

[10] James E John. *Gas Dynamics.* Allyn and Bacon, Boston, MA, 1984.

[11] Victor Streeter and E. Benjamin Wylie. *Fluid Mechanics Eighth Edition.* McGraw-Hill, New York, New York, 1985.

[12] S. Timoshenko and S. Woinowsky-Krieger. *Theory of Plates and Shells.* McGraw-Hill, New York, New York, 1987.

[13] V. Mcneil, S. Wang, and M Schmidt. Issues regarding the application of the electrochemical etch-stop technique to fabricate microstructures using wafer bonding. In *Proceedings for the First International Symposium on Semiconductor Wafer Bonding: Science, Technology and Applications*, pages 180–189, Phoenix, AZ, October 1991.

[14] Lalitha Parameswaran. Silicon pressure sensor using wafer bonding technology. Master's thesis, Massachusetts Institute of Technology, Cambridge, MA, September 1993.

[15] David Moser. *CMOS Flow Sensors.* PhD thesis, Swiss Federal Institute of Technology, Zurich, Switzerland, 1993.

[16] D.K. Cohen and R Nieman. Non-contact measurement of polished silicon wafer microroughness. Technical Report 91-011, Wyko Corporation, December 1991.

[17] D McQuarrie and P Rock. *General Chemistry.* W.H. Freeman and Company, New York, New York, 1984.

[18] Y.C. Tai. Personal communication.

[19] Howard Goldberg. Personal communication.